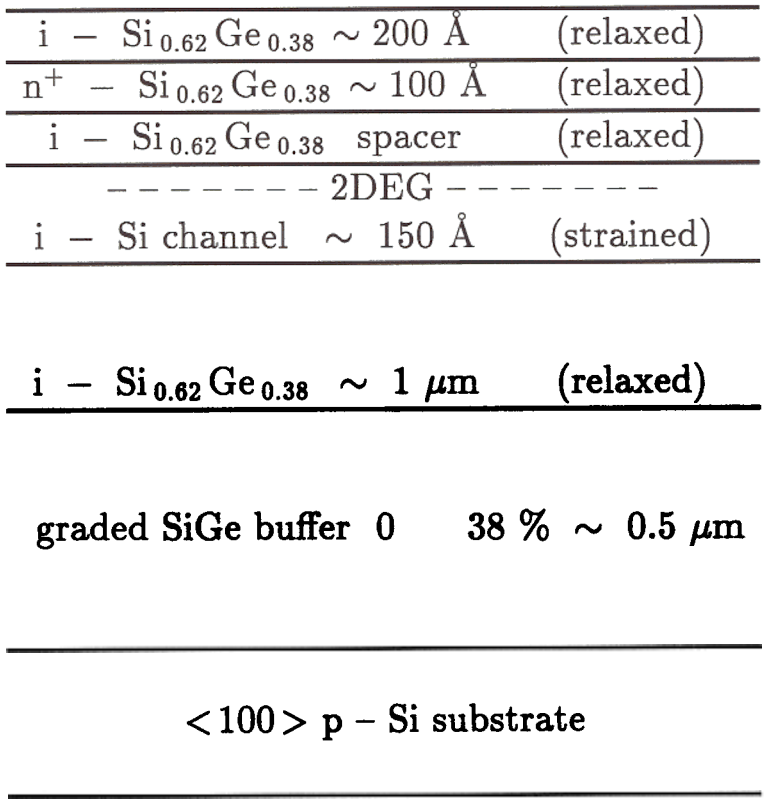

Figure 5.3: Sample structure for field effect transistors similar to Fig. 4.5. The spacer was 20 Å and the supply layer doping was reduced to 4×10^{18} cm^{-3} to ensure complete depletion by gate bias. The undoped 200 Å cap is necessary to form the low leakage Aluminum Schottky contact.

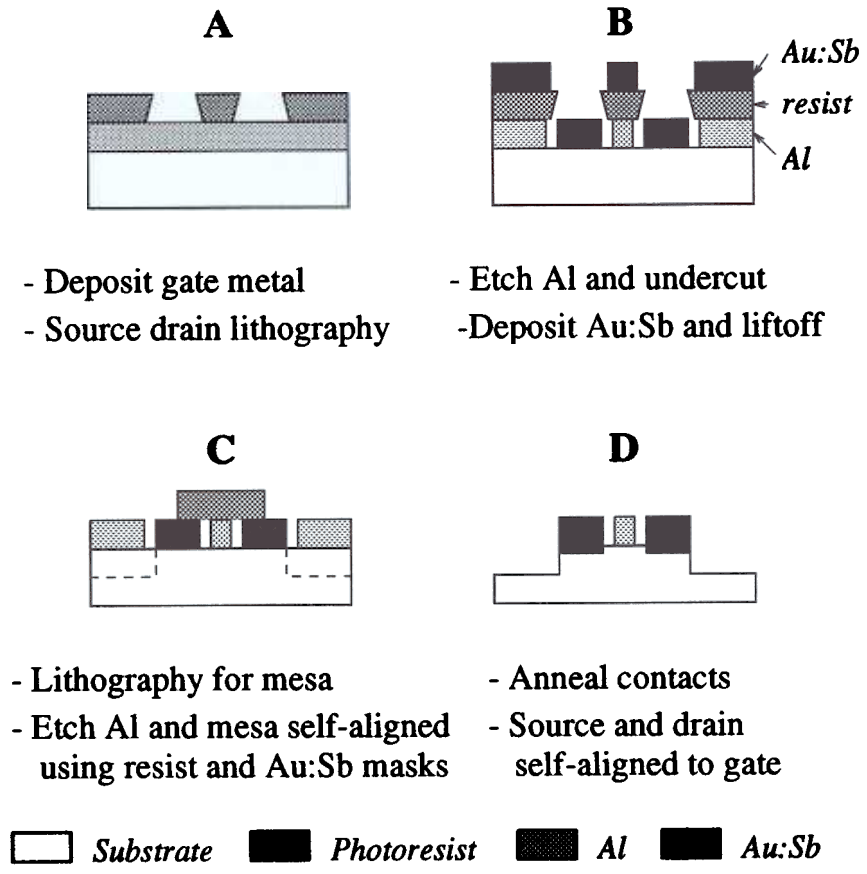

Figure 5.4: Novel two-mask processing scheme for modulation doped field effect transistors. The first lithography step (A and B) forms the source and drain contacts self-aligned to the gate contact by overetch under the resist. The second lithography step (C and D) isolates the device by a mesa etch self-aligned to the source and drain metal contacts.

from the source and drain regions and overetched slightly underneath the resist to separate the gate metal. The contact metal 50 Å Au/1500 Å Au:Sb/1000 Å Au is evaporated and lifted off using the *same* resist pattern. This forms the source and drain contacts self-aligned to the gate. The gate-source and gate-drain separation can be accurately and reproducibly controlled to less than 2 μm . The second lithography step protects the gate metal and the exposed gaps between source, drain and gate contacts. Finally the aluminum is etched away from the rest of the sample, followed by a mesa etch, self-aligned to the source and drain, using the resist and the Au:Sb contacts as masks. After numerous trials, a solution consisting of 800 ml HNO_3, 800 ml HBF_4 and 1 g NH_4BF_4 was found to be a suitable chemical etchant ($\sim$ 3000 Å /min) that does not attack Au or photoresist. After the isolation etch, the Au:Sb is annealed 330–370 °C for 10 min in a forming gas atmosphere to form the ohmic contacts to the 2DEG. This annealing step does not degrade gate characteristics and induce more leakage.

5.4 FET Characteristics

The devices were characterized at room temperature and low temperature (79 K) in a temperature-controlled probe station and the data was recorded on a HP4145B semiconductor parameter analyzer. Typical I-V characteristics for a device with a 5μm x 125 μm gate area, 2 μm source-gate and drain-gate separations, and 300 Å gate-channel separation are shown in Fig. 5.5. The threshold voltage of this device was $\sim$ -1 V and enhancement mode operation upto 200 mV could be achieved. The maximum carrier density and the mobility in the channel is estimated to be 1×10^{12} cm^{-2} and 1000 $cm^2/V \cdot s$ respectively which compares well with the Van der Pauw data. In other devices, the Schottky gate could be forward biased upto 600 mV before significant leakage ($>$ 10 μA at V_G 1 V for 100 $\times$ 100 μm^2 gate areas) was

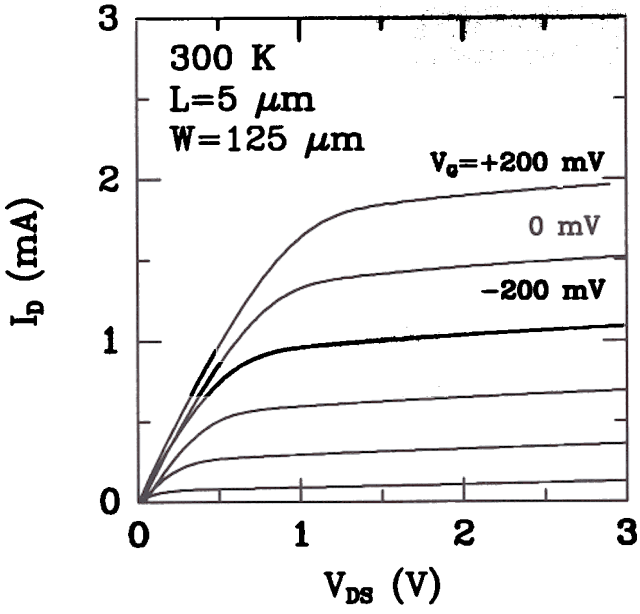

Figure 5.5: Drain current (I_D) as a function of source-drain bias (V_{DS}) of a typical FET for different gate voltages (V_G) in steps of 200 mV. The gate area was 5 μm x 125 μm and separated by 2 μm from source and drain. The threshold voltage is $\sim$ -1 V.

observed. In all devices the gate current was below 0.1 A/cm^2 for $V_G = -1$ V at 300 K, significantly lower than previous reports [48, 49]. This can be attributed to the good n-type dopant turn-off profiles obtained in our reactor. However the maximum transconductance observed for 5 μm gate lengths was only 20 mS/mm at room temperature which increased to 30 mS/mm at 79 K. These numbers did not improve for shorter gate lengths down to 2 μm . Detailed analysis of the data from devices with varied geometry indicated that parasitic contact resistances were responsible for the low transconductance.

For a long channel FET in the linear regime, the drain current (I_D) is proportional to the source-drain bias (V_{DS}):

$$\rho_{DS} \equiv \frac{V_{DS}W}{I_D} = (\rho_S + \rho_D) + R_{channel}(V_G - V_T)L \tag{5.1}$$

where ρ_{DS} is the specific source-drain resistance (per unit gate width), ρ_S is the specific source access resistance (including source contact resistance), ρ_D is the specific drain access resistance (including drain contact resistance), $R_{channel}(V_G)$ is the channel resistance (in $\Omega/\square$) modulated by the gate voltage V_G above the threshold V_T, and L and W are the gate length and width respectively. A plot of ρ_{DS} as a function of the the gate length L should therefore yield a straight line with the parasitic resistance $(\rho_S + \rho_D)$ as the intercept. Fig. 5.6 shows experimental data for four devices with different gate lengths and widths but otherwise similar. The contacts were annealed at two different temperatures. From the intercept, we obtain a value of 40 Ωmm as the parasitic resistance for the 330 °C anneal. This number reduces to 25 Ωmm if the annealing temperature is raised to 370 °C but annealing at higher temperatures does not lead to further improvement. This relatively high parasitic resistance can be attributed to the contacts and limits the maximum extrinsic transconductance observable in these devices to less than 40 mS/mm.

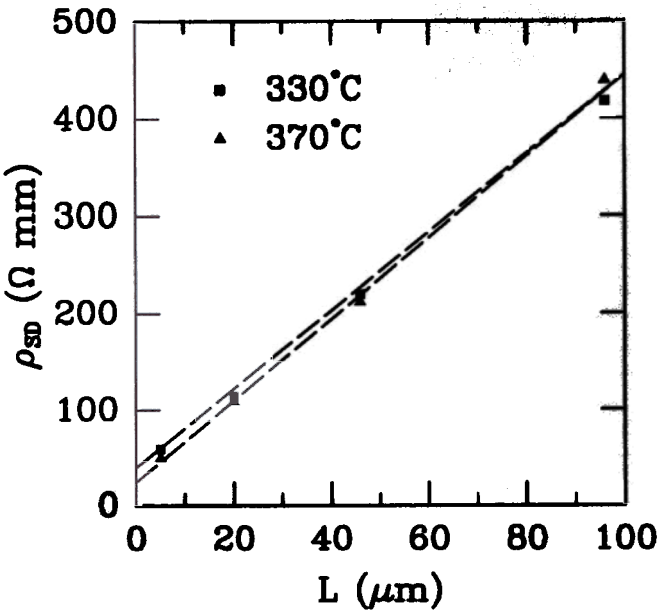

Figure 5.6: Specific source-drain resistance ρ_{DS} (per unit gate width) as a function of the gate length L for four devices with gate lengths 5 μm (W=125 μm), 20 μm (W=125 μm), 45 μm (W=225 μm) and 100 μm (W=325 μm) with 2 μm source (or drain) to gate separation. The contacts (area 100 μm x 100 μm) were annealed at two different temperatures for 10 minutes.

5.5 Conclusions

In summary, we fabricated MODFETs with low gate leakage currents (< 0.1 A/cm^2) and enhancement mode operation (upto +600 mV) at room temperature using a simple two-mask process. The transconductance was however limited by parasitic contact resistances. This might be improved by incorporating heavily doped regions underneath the contact areas either by *in situ* growth or ion implantation. High performance enhancement mode MODFETs with low gate currents at 300 K and transconductances reaching 390 mS/mm have been recently reported by the IBM group [51].

Chapter 6

Alloy scattering in SiGe quantum wells

Introduction

At the end of Chap. 3 we speculated on the possibility of alloy scattering being the dominant scattering mechanism which limits the maximum low temperature mobilities of holes in the strained $Si_{1-x}Ge_x$ channels. The modulation doped structure at low temperature is an ideal test-bed for establishing this conclusively because other mechanisms like phonon scattering and impurity scattering can be suppressed, if not entirely eliminated, in favor of alloy scattering. Alloy scattering was studied many years ago in *bulk* $Si_{1-x}Ge_x$ alloys and an alloy scattering potential of 0.5 eV was derived for electrons [52]. However those measurements were carried out at higher temperatures (100–300 K), where all three energy-dependent mechanisms, phonon, impurity and alloy were equally important and extracting the alloy potential was prone to error. Furthermore, it is not clear if this value is directly applicable to *two-dimensional, strained* $Si_{1-x}Ge_x$ systems.

Theoretical basis for alloy scattering

The simplest theoretical approach to alloy scattering is based on the "virtual crystal" model for random alloys which works well for semiconductor alloys composed of

similar isovalent atoms [6]. This procedure was described briefly in Chap. 2.3. aperiodic crystal potential V_C can be written as:

$$V_C(\mathbf{r}) = \sum_{\mathbf{R}_{Si}} V_{Si}(\mathbf{r} - \mathbf{R}_{Si}) + \sum_{\mathbf{R}_{Ge}} V_{Ge}(\mathbf{r} - \mathbf{R}_{Ge})$$

where V_{Si} and V_{Ge} are the atomic potentials of Si and Ge atoms respectively. Strictly speaking these potentials should be considered as the one electron pseudopotentials seen by the valence electrons. If the atoms are similar, like Si and Ge, the crystal potential can be decomposed into a periodic "virtual crystal" potential $V_{virtual}$,

$$V_{virtual}(\mathbf{r}) = \sum_{all\ \mathbf{R}} (1-x)V_{Si}(\mathbf{r} - \mathbf{R}) + xV_{Ge}(\mathbf{r} - \mathbf{R})$$

and a "disorder" potential V_{dis},

$$V_{dis}(\mathbf{r}) = \sum_{\mathbf{R}_{Si}} -x\delta V(\mathbf{r} - \mathbf{R}_{Si}) + \sum_{\mathbf{R}_{Ge}} (1-x)\delta V(\mathbf{r} - \mathbf{R}_{Ge})$$

where

$$\delta V(\mathbf{r}) = V_{Ge}(\mathbf{r}) - V_{Si}(\mathbf{r})$$

This procedure is depicted schematically in Fig. 6.1. The virtual crystal has a strain configuration identical to the actual crystal with the same atomic volume Ω_0 and can be described by standard band theory with Bloch wavefunctions $\Phi_{n,\mathbf{k}}(\mathbf{r}) \sim u_{n,\mathbf{k}}(\mathbf{r})\exp(i\mathbf{k}\cdot\mathbf{r})$ and energy dispersion $E(\mathbf{k})$. The disorder potential can be treated as the perturbation that causes scattering among the Bloch states of the virtual crystal. This model can be further simplified by replacing the disorder potential in each unit cell with a weighted average delta function:

$$V_{dis}(\mathbf{r}) = \sum_{\mathbf{R}_{Si}} -x\Omega_0 V_{alloy}\delta(\mathbf{r} - \mathbf{R}_{Si}) + \sum_{\mathbf{R}_{Ge}} (1-x)\Omega_0 V_{alloy}\delta(\mathbf{r} - \mathbf{R}_{Ge})$$

where

$$V_{alloy} = \frac{1}{\Omega_0}\int_{\Omega_0} \delta V(\mathbf{r}) u^*{}_{n,\mathbf{k}}(\mathbf{r}) u_{n,\mathbf{k}}(\mathbf{r}) \mathrm{d}^3 r$$

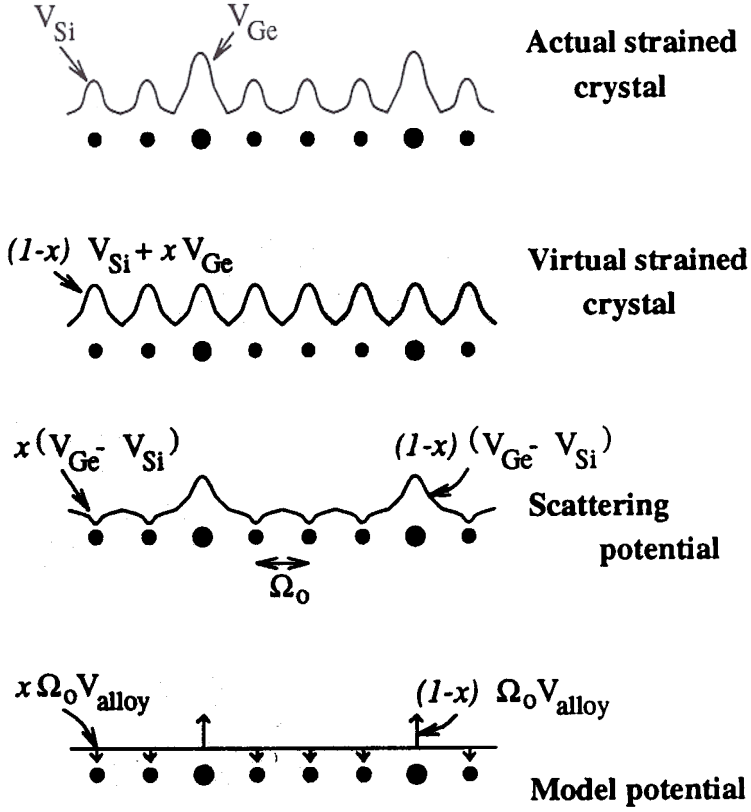

Figure 6.1: The virtual crystal model for a hypothetical one-dimensional random string of Si and Ge atoms with average Ge composition of 25% and strained volume per atom Ω_0. The actual random potential of the strained crystal is decomposed into a periodic potential of a strained virtual crystal with the same atomic volume and a fluctuating random disorder potential which is treated as a perturbation.

is the effective alloy scattering potential which acts only on the envelope functions. Using Eqn. 6.5 and the two-dimensional envelope functions given by Eqn. 2.1, we obtain the average square alloy matrix element and the alloy mobility given by Eqns. 2.22 and 2.23.

The strain is incorporated in this model only through the alloy scattering potential V_{alloy} defined by Eqn. 6.6. Both the periodic Bloch functions of the strained virtual crystal and the one-electron atomic pseudopotentials depend on strain. However the magnitude of these effects cannot be calculated from theory at this point. In unstrained material systems, V_{alloy} for electrons has frequently been estimated as the difference between conduction band edges of the constituent atoms [6, 53]. In the next few sections we extract this parameter for strained $Si_{1-x}Ge_x$ alloys through experiments.

6.3 Experimental study

From the theoretical expression for alloy scattering limited mobility (Eqn. 2.24), we infer that a weak dependence of the experimental mobility on carrier density ($\mu_{alloy} \sim n^{-1/3}$) and a stronger dependence on the germanium content ($\mu_{alloy} \sim x(1-x)$) are the two signatures of alloy scattering limited transport. The theoretical alloy mobility is most sensitive to the germanium content x for small x where it decreases rapidly from infinity for $x = 0$ (no alloy scattering) to a finite value for $x > 0$, and one would therefore like to concentrate experiments in this region. This regime is however inaccessible for the 2DHG structures of Chap. 3 with pure Si barriers, because little or no carrier transfer occurs for $x \rightarrow 0$. We therefore use the 2DEG structures of Chap. 4 with $Si_{0.62}Ge_{0.38}$ barriers.

6.3.1 Sample structures

Four samples were grown by RTCVD with strained $Si_{1-x}Ge_x$ channels but otherwise similar to Fig. 4.5. The germanium content in the channel was varied from 0% to 20% and a large spacer thickness of 100 Å was used to eliminate remote impurity scattering. The sample structures are shown in Fig. 6.2. In order to convince ourselves that any mobility degradation due to adding germanium in the channel is not caused by some extraneous impurities in our germane source, we also studied two samples (with 0 and 10% Ge in the channel) grown by MBE at AT&T Bell Laboratories by Dr. Ya-Hong Xie. These samples used an Sb delta- doped layer for carrier supply, a 200 Å spacer and only 30% germanium in the relaxed buffer and barriers. The MBE structure is also shown in Fig. 6.2. All samples have similar band structure as shown in Fig. 4.1 but varying amounts of germanium *and* strain in the channel.

6.3.2 Hall measurements

Temperature dependent Hall measurements were carried out using Van der Pauw geometry with annealed Au:Sb contacts as described in Chap. 4. The results for three RTCVD samples are displayed in Fig. 6.3. All samples showed typical modulation doping behaviour. As observed in Chap. 4 the as-grown RTCVD samples exhibited some parallel conduction at low temperature (especially the $x > 0$ samples because of the reduced carrier transfer) which was removed by etching the cap layer. The MBE samples did not have this problem because of the smaller number of integrated supply dopants provided by delta-doping. The low temperature (10 K for RTCVD and 4.2 K for MBE) Hall results for all samples are summarised in Table. 6.1. The last two columns are calculated mobilities described below. The peak low temperature mobility is strongly degraded with increasing Ge content in the channel, as expected for alloy scattering dominated transport. A small part of the degradation is due to loss of screening of impurities since, for larger x, the smaller conduction band offset

RTCVD

$n^+ - Si_{0.62}Ge_{0.38} \sim 300$ Å (relaxed)
$Si_{0.62}Ge_{0.38}$ spacer (relaxed)
- - - - - - - 2DEG - - - - - - -
i – $Si_{1-x}Ge_x$ channel ~ 75 Å (strained)
graded SiGe buffer 0 – 38 % ~ 0.5 μm

MBE

i – $Si_{0.7}Ge_{0.3} \sim 500$ Å (relaxed)
Sb δ – doping 1.5×10^{12} cm^{-2}
i – $Si_{0.7}Ge_{0.3}$ spacer (relaxed)
- - - - - - - 2DEG - - - - - - -
i – $Si_{1-x}Ge_x$ channel ~ 100 Å (strained)
graded SiGe buffer 0 – 30 % ~ 3 μm

Figure 6.2: Samples grown by RTCVD and MBE for alloy scattering studies. The structures are similar to those in Chap. 4. The RTCVD samples used 100 Å spacers and $\sim 2 \times 10^{19}$ cm^{-3} caps with $Si_{1-x}Ge_x$ channels (0%–20%) grown at 625 °C . The MBE samples used 200 Å spacers with $Si_{1-x}Ge_x$ channels (0% and 10%) grown at 650 °C .

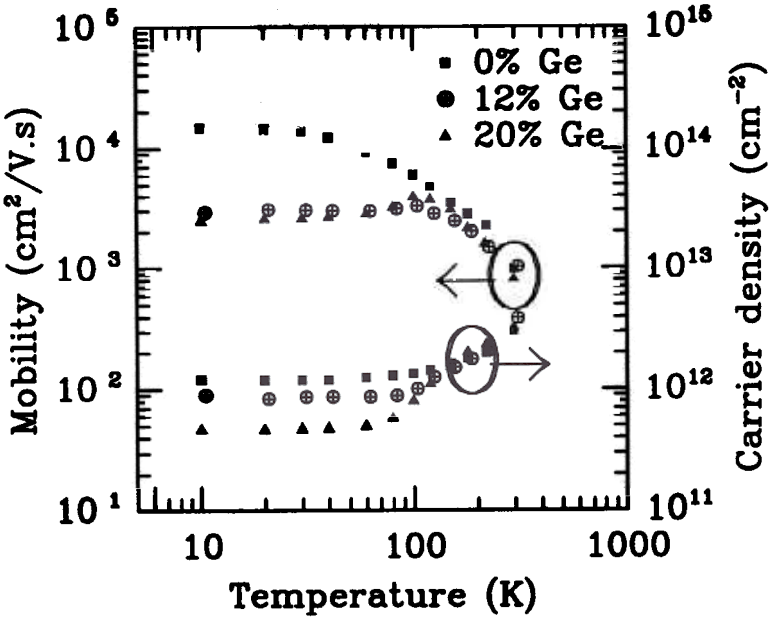

Figure 6.3: Temperature dependent mobility and carrier density for the RTCVD samples with germanium contents 0,12 and 20% in the channel. Sample structure is shown in Fig. 6.2. All samples show typical modulation doping behaviour. Note that peak low temperature mobilities are substantially degraded with alloying.

Sample #	Grown by	x	n (10^{11} cm^{-2})	μ_{meas} (cm^2/Vs)	μ_{imp} (cm^2/Vs)	μ_{alloy} (cm^2/Vs)
1341	RTCVD	0.00	12.0	20000	20000	...
1381	RTCVD	0.06	14.0	6420	21600	9130 ± 30%
1343	RTCVD	0.12	8.8	3000	17130	3640 ± 16%
1344	RTCVD	0.20	4.7	2500	12520	3120 ± 18%
x345	MBE	0.00	3.5	27700	27700	...
x346	MBE	0.10	1.4	3000	4300	9740 ± 60%

Table 6.1: Summary of carrier density n and mobility μ_{meas} for different samples with strained $Si_{1-x}Ge_x$ channels. The RTCVD data was measured at 10 K while the MBE data was taken at 4.2 K. Sample # 1381 had a smaller spacer (40 Å) and doping ($\sim 5 \times 10^{18}$ cm^{-3}) than shown in Fig. 6.2. The last two columns are the calculated mobilities due to impurity scattering μ_{imp} and alloy scattering μ_{alloy} .

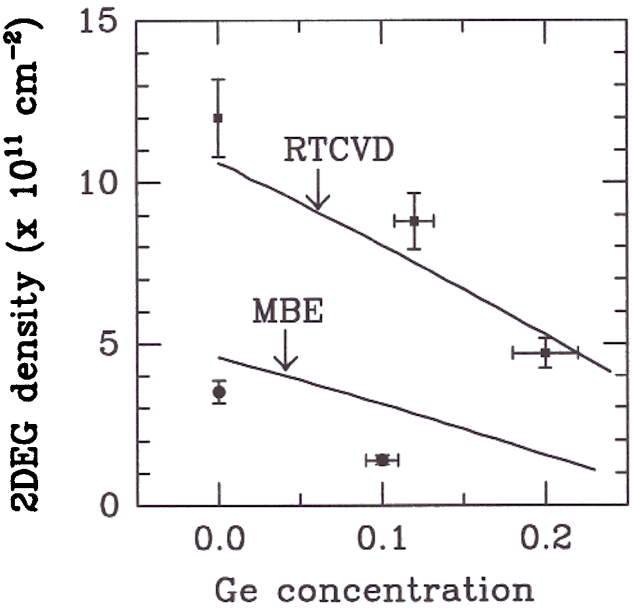

Figure 6.4: Calculated equilibrium carrier density for the RTCVD and MBE structures shown in Fig. 6.2. Theoretical band offsets as calculated by Van de Walle *et. al.* [10] were used. The experimental points are from Table. 6.1.

between the barrier and the $Si_{1-x}Ge_x$ channel results in smaller carrier transfer. Calculations of the equilibrium carrier density for the RTCVD and MBE structures are shown in Fig. 6.4 along with the experimental data. The carrier transfer in the MBE samples is smaller than the RTCVD samples because of the lower germanium content in the buffer and the larger spacer thickness. The RTCVD data agrees well with the calculation (within experimental error) while the MBE data are consistently 30–50% lower than the theoretical curve. The difference could be the depletion charge ($\sim 1 \times 10^{11}$ cm^{-2} for a background doping of 1×10^{15} cm^{-3}), which was neglected in the calculation and becomes important at these low densities.

6.3.3 Extraction of the alloy scattering potential

In order to estimate the alloy scattering potential, it is necessary to extract the mobility limited by alloy scattering (μ_{alloy}) from the measured mobilities (μ_{meas}). We

assume that $\mu_{meas}{}^{-1} = \mu_{imp}{}^{-1} + \mu_{alloy}{}^{-1}$ where μ_{imp} is the mobility limited by impurity and all other scattering mechanisms. The value of μ_{imp} can be obtained from the $x = 0$ samples because there is no alloy scattering. Assuming the spatial density of impurities has not changed appreciably for the $x > 0$ samples (identical structures grown mostly consecutively), we can use the same μ_{imp} but scaled with respect to carrier density n. For the RTCVD structures, we know from the calculations of Fig. 4.12 that, for a spacer thickness of 100 Å , the mobilites are limited by background doping. Similar calculations indicate that, for the MBE samples with low background doping ($< 10^{15}$ cm^{-3}), the mobilities are limited by remote impurity scattering. We use the theoretical $\mu_{imp} \sim n^{0.5}$ for background impurity and $\mu_{imp} \sim n^{1.5}$ for remote impurity scaling laws to calculate μ_{imp} for the $x > 0$ samples and extract μ_{alloy} . These results are displayed in the last two columns of Table. 6.1 The error bars reflect possible changes in the impurity density by a factor of 2 from sample to sample. The MBE data has significantly more error because of the large impurity scattering component.

The alloy scattering model was presented earlier in Sec. 6.2. In that derivation, a completely random alloy (no ordering) with a simple one-valley band and only intravalley scattering was assumed. In our samples, there are two valleys in the strained $Si_{1-x}Ge_x$ channel which are degenerate in energy. The short range nature of the alloy scattering potential should effectively couple states with large differences in the crystal momentum $\Delta\mathbf{K}$ (see Fig. 6.5). It is therefore expected that intervalley scattering and intravalley scattering due to alloy effects are comparable in magnitude, increasing the available final states into which electrons may be scattered. This will lower the mobility by a factor equal to the degeneracy of the band minimum g_v. We finally obtain

$$\mu_{alloy} \quad \frac{e\hbar^3}{g_v\, m_{xy}^2 \Omega_0 V_{alloy}^2\, x(1-x)} \left(\frac{16}{3b}\right) \equiv \frac{K}{V_{alloy}^2\, x(1-x)\, n^{\frac{1}{3}}}$$

where Ω_0 is the atomic volume ($= a_{\|}^2 a_{\perp}/8$, $a_{\|}$ and $a_{\perp}$ are the parallel and perpen-

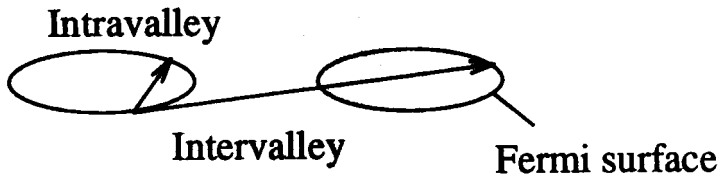

Figure 6.5: Schematic diagram showing intervalley scattering due to the short ranged alloy potential. The number of available final states for scattering increases, reducing the alloy mobility.

dicular lattice constants) and b is the variational parameter defined in Eqn. 2.6. The transverse effective mass m_{xy} in strained $Si_{1-x}Ge_x$ alloys has not yet been determined experimentally. In pure Si channels, cyclotron resonance experiments indicate an effective mass of $0.19m_0$, close to the Si bulk value [17]. We can therefore assume that the strain does not change the band curvatures to first order. In the following calculations, we use $m_{xy} = (0.19 + 0.10x)m_0$ as an interpolation between bulk Si and bulk Ge transverse masses at the Δ-point. Eqn. 6.7 has been evaluated and plotted in Fig. 6.6 in such a way that the slope corresponds to the alloy potential in eV. The data can be best fit by $V_{alloy} = 0.8 \pm 0.1$ eV. This value is different from ~ 0.5 eV measured for *bulk* $Si_{1-x}Ge_x$ alloys [52] and could be due to the effect of strain. In Fig. 6.6, we assumed V_{alloy} is constant even though the strain changes with Ge content in the channel. The resolution and the number of data points in the experiment is, however, insufficient to detect a change in V_{alloy} as we approach the unstrained limit $x \rightarrow 0$. More experiments with smaller Ge contents (1–5%) might resolve this issue. As mentioned before, in other unstrained material systems, V_{alloy} for electrons was estimated to be the conduction band offset between the constituent elements of the alloy [6, 53]. Although in our case V_{alloy} is close to the difference in Si-like Δ-point conduction band edges between strained Si and strained Ge on the relaxed $Si_{0.62}Ge_{0.38}$ substrate (~ 0.7 eV from Fig. 4.10), it is best treated as an empirical parameter at this point due to the complicated nature of the strained indirect bands.

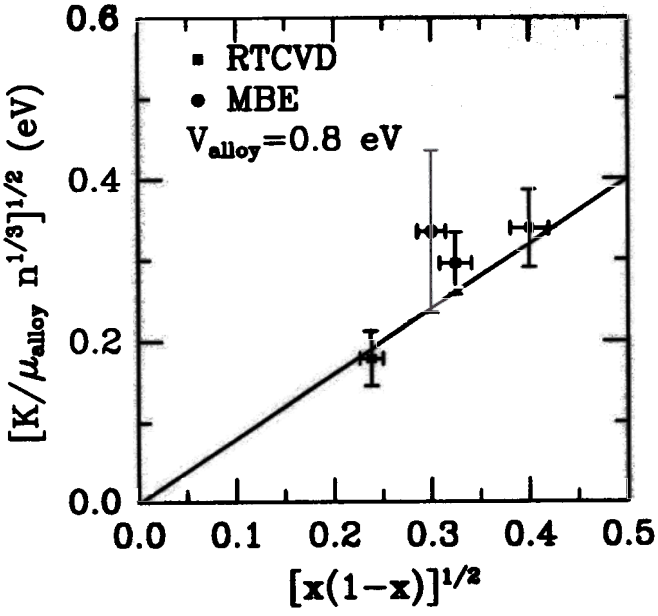

Figure 6.6: Alloy scattering model calculations displayed with V_{alloy} as an independent parameter. K is a material dependent parameter defined by Eqn. 6.7, while μ_{alloy} , n and x are experimental values from Table. 6.1. The data (ignoring the MBE point with large error) is best fit by $V_{alloy} = 0.8 \pm 0.1$ eV.

Gating experiments

The second signature of alloy scattering is its weak dependence on carrier density, in contrast to impurity scattering. In this section, we discuss experimental results for the mobility as a function of carrier density using gated Hall bars.

Sample structure

The RTCVD structures studied in Sec. 6.3 could not be themselves used for Schottky gating experiments because of the heavily doped cap. Hence the RTCVD MODFET structure shown in Fig. 5.3 was used. After a few unsuccessful attempts where the doping was either too high for complete depletion or too low for adequate carrier transfer, a structure consisting of a 400 Å undoped cap, a 100 Å $\sim 3 \times 10^{18}$ cm^{-3} supply layer and a 40 Å spacer proved to be a success. Two samples with 0% Ge (sample # 1109) and 12% Ge (sample # 1395) strained channels were studied. The reduced spacer resulted in maximum carrier transfer, but the mobility in the pure Si channel was now limited by remote impurity scattering. The growth details of all samples are given in Appendix C.

6.4.2 Gated Hall measurements

The Hall bars were processed in three simple steps, similar to the MODFET process shown in Fig. 5.4. First Au:Sb was thermally evaporated, lifted off and annealed to form ohmic contact pads. The pads were then covered with resist and the gate metal, 1000 Å Al, was evaporated and lifted off. Finally the mesa pattern was defined followed by an Al etch and a mesa isolation etch. This process self-aligns the gate to the mesa edge.

Fig. 6.7 shows the measured carrier density at 10 K as a function of the gate bias. Forward gate biases upto 400 mV were possible before significant leakage occured

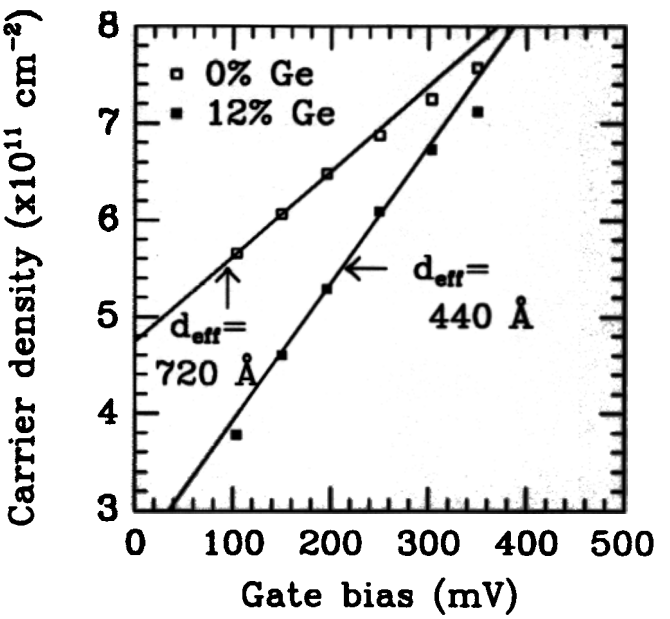

Figure 6.7: Dependence of carrier density on gate voltage from Hall measurements at 10 K for 0% (# 1109) and 12% (# 1395) devices. Enhancement mode operation up to 400 mV can be achieved before the data deviates from linearity due to leakage. The effective gate to channel distance d_{eff} is given by the slope in the linear region.

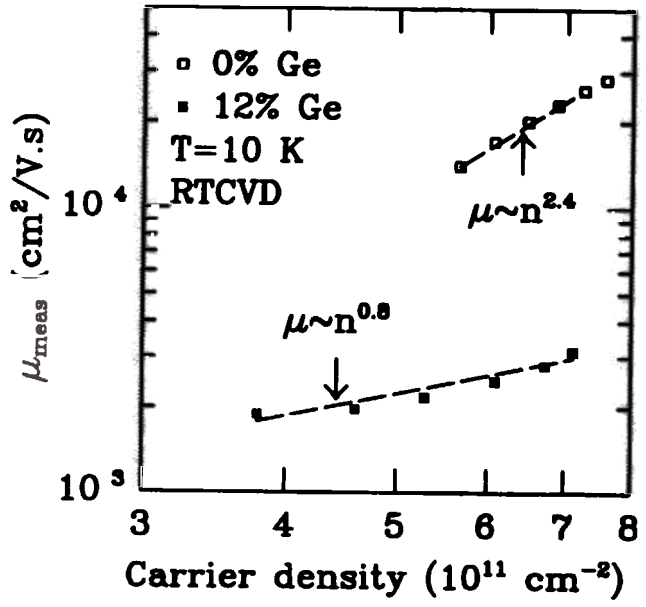

Figure 6.8: Hall mobility as a function of carrier density for the gated Hall bars. The 0% sample shows strong dependence ($\mu \sim n^{2.4}$) characteristic of remote impurity scattering while the 12% sample shows much weaker dependence. The reduced slope is evidence of alloy scattering.

From the linear region, an effective gate to channel distance of 720 Å for the 0% device and 440 Å for the 12% device were determined. The deviation from the intended 500 Å separation could be due to variations in the growth rate. The mobility was also measured simultaneously and the results ($\mu \sim n^{\gamma}$) are displayed in Fig. 6.8 as a function of carrier density.

6.4.3 Comparisons with theory

The mobility of the 0% sample shows a strong dependence on density, characteristic of remote impurity scattering. The value of the exponent, $\gamma = 2.4$, is close to that normally observed in AlGaAs/GaAs modulation doped structures ($\gamma = 1.5 - 2.0$) [54], but higher than the theoretical value of 1.5. The reason for this is not clear and more data is required before a valid theory can be proposed. However the 12%

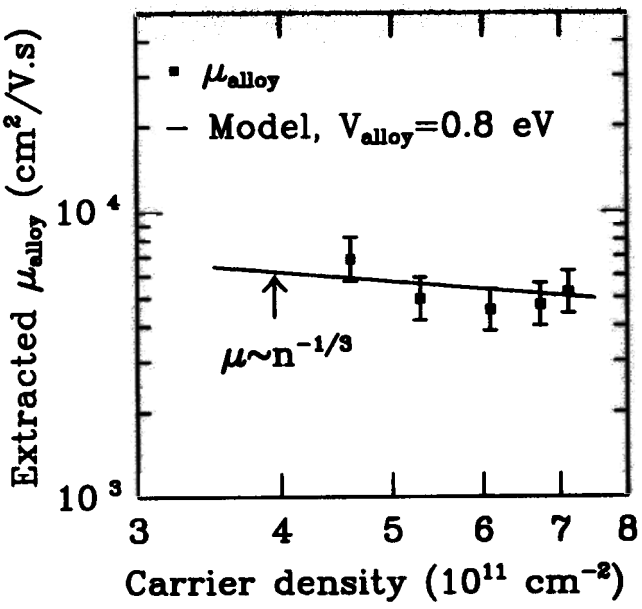

Figure 6.9: Extracted alloy scattering limited mobilities μ_{alloy} after subtracting out the impurity limited mobilities μ_{imp} from the measured data μ_{meas} . The data fits the alloy scattering model well with V_{alloy} =0.8 eV.

Ge sample clearly shows a much weaker dependence with $\gamma \sim 0.8$. Although we expect $\gamma = -1/3$ for pure alloy scattering, this weak negative dependence is masked by the much stronger positive dependence of the impurity scattering component in our samples. To prove this, we show in Fig. 6.9, the mobilities limited purely by alloy scattering for the 12% Ge sample, after subtracting the strong density-dependent ($\gamma = 2.4$) impurity component from the measured data. The extracted mobilities show the expected $\mu_{alloy} \sim n^{-1/3}$ dependence and agree in magnitude with the alloy scattering model using V_{alloy} =0.8 eV. This confirms alloy scattering limited transport in our strained $Si_{1-x}Ge_x$ channels.

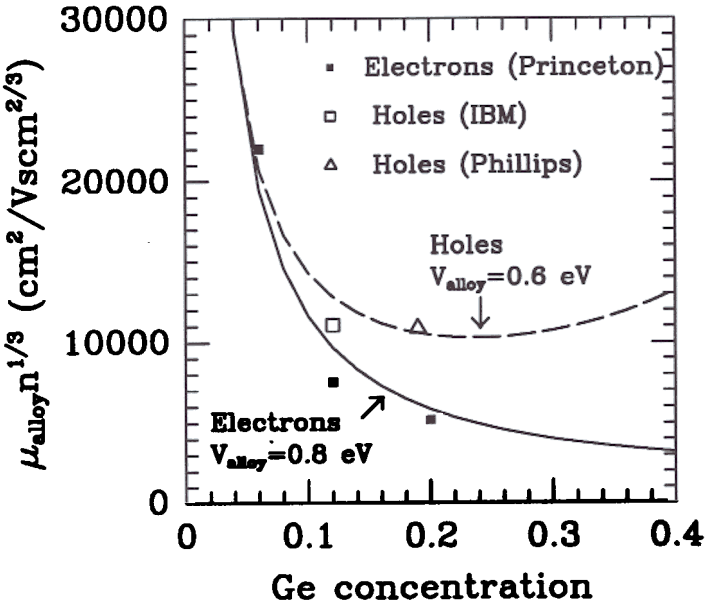

Figure 6.10: Calculated μ_{alloy} (in $cm^2/V \cdot s$) for electrons (V_{alloy} =0.8 eV) and holes (V_{alloy} =0.6 eV), normalized by the carrier concentration (in 10^{11} cm^{-2}) as a function of germanium content. The solid squares are experimental data from Table. 6.1 while the open symbols represent maximum low temperature hole mobilities reported in references [30] and [29].

6.5 Alloy scattering of holes

In order to explain the poor hole mobilities of 2DHGs in strained $Si_{1-x}Ge_x$ channels, we invoke the alloy scattering model described above. No intervalley scattering should be included since the normally degenerate valence band is split by strain ($g_v = 1$). For the hole effective masses, cyclotron resonance experiments have been carried out recently [31] for a few specific germanium concentrations. The effective mass depends strongly on the germanium content and possibly on carrier density due to non-parabolicity. Here we use a linear interpolation given by $m_{xy} = (0.44 - 0.42x)m_0$ which fits the experimental cyclotron resonance data of Ref.[31]. Fig. 6.10 shows maximum low temperature hole mobilities (normalized by the carrier density) reported in literature for strained $Si_{1-x}Ge_x$ layers on Si substrates [30, 29] along with the model

calculation. The results fit well for an alloy scattering potential of 0.6 eV, assuming other mechanisms are insignificant. For comparison, the calculations for electrons with V_{alloy}=0.8 eV are also displayed in the same figure. That V_{alloy} for holes is less than that for electrons is not totally unexpected. A similar trend has been observed in III-V alloys [53]. From a theoretical standpoint too, one would use the *valence* band Bloch functions of the virtual crystal in Eqn. 6.6 instead of the conduction band functions, and obtain different V_{alloy} for electrons and holes. Furthermore the strain configuration for holes is compressive as compared to tensile for electrons.

6.6 Further implications of alloy scattering

In this section, we present three interesting ideas linked with alloy scattering. These are preliminary results only and no attempt is made at rigorous justification. Indeed more experimental evidence and theoretical work are required before their validity can be established beyond doubt.

6.6.1 Photoluminescence of $Si_{1-x}Ge_x$ strained alloys

Since 1991 when the first band-edge photoluminescence results from strained $Si_{1-x}Ge_x$ quantum wells were reported [14], there has been extensive experimental activity in this area [55]. Much of the motivation stems from the quest for optical emission devices from Si-based systems. Typical photoluminescence (PL) spectra at 77 K from a set of $\sim$ 100 Å $Si_{1-x}Ge_x$ quantum wells grown on $< 100 >$ Si substrates with varying Ge content are shown in Fig. 6.11. Two prominent peaks originating from a "no-phonon" transition (NP) and a TO-phonon assisted transition in the indirect $Si_{1-x}Ge_x$ quantum well can be clearly observed. At lower temperatures, individual Si-Si, Si-Ge and Ge-Ge phonons can be well resolved [14]. For optical devices, apart from emission wavelength, the emission intensity is also an important criterion. The

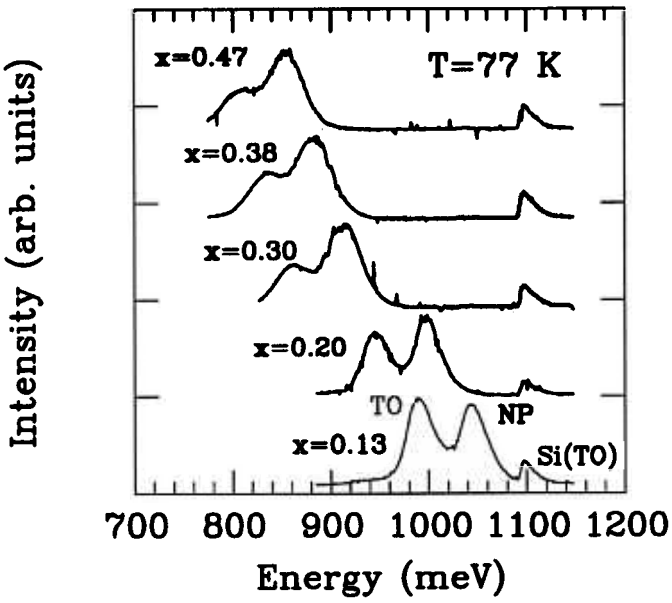

Figure 6.11: Photoluminescence spectra at 77 K from a series of $\sim$ 100 Å $Si_{1-x}Ge_x$ strained quantum wells grown on $<100>$ Si substrates with different Ge content. The substrate peak denoted by Si stays fixed in energy while the $Si_{1-x}Ge_x$ "no-phonon" (NP) and phonon replica (TO) move to lower energies with alloying. The ratio of intensities, I_{NP}/I_{TO} increases with x.

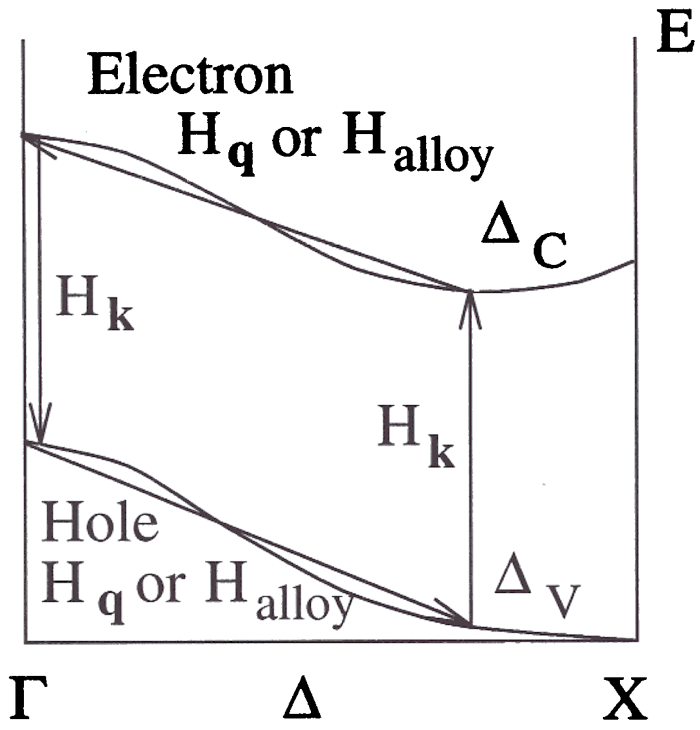

Figure 6.12: Schematic diagram of indirect radiative transitions in $Si_{1-x}Ge_x$ alloys. The energy of the conduction and valence bands are plotted along the $< 100 >$ direction in the Brillouin zone. Intraband transitions can be caused by either phonon scattering (H_q) or alloy scattering (H_{alloy}). Interband transitions are caused by photon perturbations (H_k).

no-phonon peak at 77 K is believed to arise solely from alloy scattering which supplies the necessary momentum to complete the indirect transition[1]. In this section, we attempt to draw a quantitative link between the alloy scattering measurements from transport and the strength of the no-phonon photoluminescence line.

Fig. 6.12 is a schematic diagram showing all possible transitions in these alloys. The band-to-band transition occurs due to perturbation of the crystal Hamiltonian by photons (H_k) which provides negligible momentum change. The actual momentum conservation is taken care by the intraband transitions involving phonon (H_q) or

[1]At lower temperatures like 4.2 K, other mechanisms like exciton localisation by impurities exist which can cause a "no-phonon" peak even in pure Si samples.

alloy (H_{alloy}) perturbations. Using standard second-order perturbation theory [7], the radiative transition rates are proportional to:

$$I_{TO} \sim \left| \underbrace{\frac{<\Delta_c|H_{\mathbf{q}}|\Gamma_c><\Gamma_c|H_{\mathbf{k}}|\Gamma_v>}{E(\Delta_c)-E(\Gamma_c)+\hbar\omega_{\mathbf{q}}}}_{\text{electron-phonon-photon}} + \underbrace{\frac{<\Gamma_v|H_{\mathbf{q}}|\Delta_v><\Delta_v|H_{\mathbf{k}}|\Delta_c>}{E(\Gamma_v)-E(\Delta_v)+\hbar\omega_{\mathbf{q}}}}_{\text{hole-phonon-photon}} \right|^2$$

and

$$I_{NP} \sim \left| \underbrace{\frac{<\Delta_c|H_{alloy}|\Gamma_c><\Gamma_c|H_{\mathbf{k}}|\Gamma_v>}{E(\Delta_c)-E(\Gamma_c)}}_{\text{electron-alloy-photon}} \right|^2 + \left| \underbrace{\frac{<\Gamma_v|H_{alloy}|\Delta_v><\Delta_v|H_{\mathbf{k}}|\Delta_c>}{E(\Gamma_v)-E(\Delta_v)}}_{\text{hole-alloy-photon}} \right|^2$$

The proportionality constants involve the density of states and other common material parameters. Note that the phase of the electron-phonon and hole-phonon matrix elements is important, causing constructive interference in silicon [56] (the matrix elements are summed and then squared), while the random alloy matrix elements are assumed to be averaged over all phases. To proceed further we make the following assumptions:

1. The phonon energy (~ 50 meV) can be neglected compared to the other energies in the denominators (order of eV).

2. Although the band gaps at Γ and Δ change with strain and Ge content, the ratio $\frac{E(\Gamma_c)-E(\Delta_c)}{E(\Gamma_v)-E(\Delta_v)}$ is close to the silicon value of $\frac{5}{8}$ for all x.

3. The Si-Si, Ge-Ge and Si-Ge TO phonon peaks are in the ratio $(1-x)^2 : x^2 : 2x(1-x)$ [57], so that the total integrated TO peak intensity is independent of x.

and obtain for the ratio of the no-phonon to the TO-phonon peaks

$$\frac{I_{NP}}{I_{TO}} \quad \frac{(M^e_{alloy})^2 + \frac{25}{64}(M^h_{alloy})^2}{(M^e_{phonon} + \frac{5}{8}M^h_{phonon})^2}$$

where $M^{e}_{alloy}(=<\Delta_c|H_{alloy}|\Gamma_c>)$ and $M^{h}_{alloy}(=<\Gamma_v|H_{alloy}|\Delta_v>)$ are the electron and hole alloy scattering matrix elements, and $M^{e}_{phonon}(=<\Delta_c|H_q|\Gamma_c>)$ and $M^{h}_{phonon}(=<\Gamma_v|H_q|\Delta_v>)$ are the electron and hole phonon matrix elements. For the latter we use bulk TO silicon values [2] per unit volume, $M^{e}_{phonon} = 204$ meV and $M^{h}_{phonon} = 245$ meV [59]. For the former, we can use the bulk alloy scattering matrix element per unit volume [7], since for well widths exceeding 100 Å , the $Si_{1-x}Ge_x$ layers show little confinement effects [60]:

$$<|M^{e,h}_{alloy}|^2>= x(1-x)(V^{e,h}_{alloy})^2 \qquad (6.11$$

Substituting the above expressions, we finally obtain for the intensity ratio:

$$\frac{I_{NP}}{I_{TO}} = 7.84x(1-x)(V^{e}_{alloy}{}^2 + 0.4V^{h}_{alloy}{}^2) \qquad (6.12)$$

The experimentally obtained ratios from the spectra of Fig. 6.11 are summarised in Table. 6.2 along with data from other samples. The ratios were calculated by fitting an Electron-Hole Plasma (EHP) model including broadening effects described in Ref.[15]. These ratios are plotted in Fig. 6.13 as a function of Ge content. The data can be well fitted by the expression:

$$\frac{I_{NP}}{I_{TO}} = 7.0x(1-x) \qquad (6.13)$$

Comparing this with Eqn. 6.12 and assuming $V^{e}_{alloy} \sim V^{h}_{alloy} = V_{alloy}$, we get $V_{alloy} \sim$ 0.8 eV. This agrees well with the earlier transport measurements, indicating that the same mechanism is responsible for the no-phonon photoluminescence peak.

Valley splitting in high magnetic fields

In Chap. 4 we described magnetotransport experiments on the high quality 2DEG formed in a strained Si quantum well with relaxed $Si_{1-x}Ge_x$ barriers. A valley

[2] This is another simplification because the strain splits the valence band degeneracy and changes the symmetry of the states and the phonon coupling between them. See, for example, Ref. [58].

Sample #	x	L_W Å	I_{NP}/I_{TO}
763	0.13		0.74
1326	0.20		1.00
764	0.23		1.44
766	0.30		1.67
760	0.34		1.76
769	0.38		1.41
770	0.47		1.48

Table 6.2: Summary of the no-phonon to TO-phonon intensity ratios from PL spectra at 77 K of similar samples with different Ge contents. The detector response correction (about 10% at these wavelengths) was neglected. Spectra for a few of these samples are shown in Fig. 6.11.

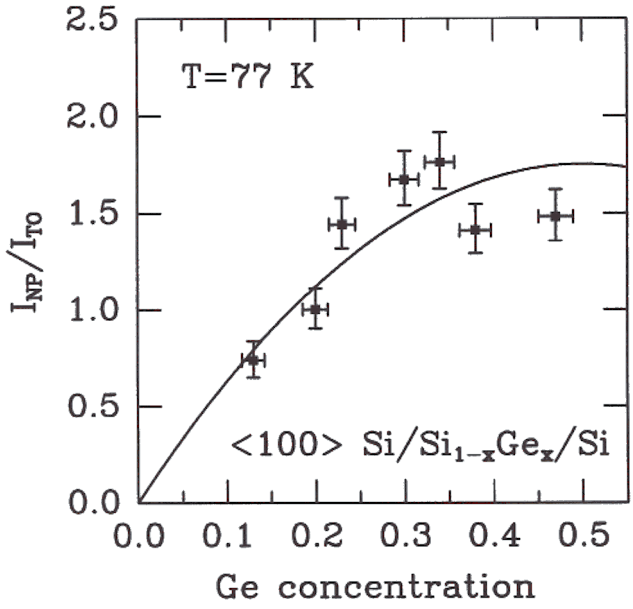

Figure 6.13: PL intensity ratios from Table. 6.2 plotted as a function of Ge content. The data can be well fitted by the expression 7.0 x(1-x).

degeneracy of 2 due to the strain was inferred from the low field data which showed only even Quantum Hall plateaus. However, at higher magnetic fields and lower densities, odd filling factors begin to appear indicating that the valley degeneracy has been lifted [61]. At a density of $\sim 2.7 \times 10^{11}$ cm^{-2} and a magnetic field of 10 T, a clear $\nu = 1$ plateau was observed [61]. Similar observations were reported recently in other many-valley systems like AlAs quantum wells modulation doped by AlGaAs barriers [62]. Valley splitting has been a controversial issue in the Si-MOS system where it was first reported many years ago [4]. A number of theories were proposed, none completely satisfactory. Some of the theories were based on sample dependent parameters like inhomogeneous strain while others invoked many-body effects. All of them, however, predict lifting of the valley degeneracy (by a few tenths of an meV) at zero magnetic field (B=0). However, the entire body of experimental evidence so far has been gathered from magnetotransport experiments involving large magnetic fields (B $\sim$ 10 T). It is therefore likely that the magnetic field plays an important role. In the following, we show how perturbations due to the alloy randomness can lift the valley degeneracy in large magnetic fields.

From the arguments involving Fig. 6.5, we know that alloy scattering strongly couples states in two different valleys with large differences in crystal momentum. We therefore expect, from first order degenerate perturbation theory, that the degeneracy is lifted by the perturbing potential with a magnitude Δ_{valley} given by:

$$\Delta_{valley} = 2\sqrt{| < \Psi_1 | H_{alloy} | \Psi_2 > |^2} = 2 < \sqrt{|M_{alloy}|^2} > \qquad (6.14)$$

where Ψ_1 and Ψ_2 are the wavefunctions of the two degenerate states, and M_{alloy} is the alloy scattering matrix element defined in Eqn. 2.22. If the channel is pure Si and the scattering occurs only in the relaxed $Si_{1-x}Ge_x$ barrier, the matrix element gets correspondingly diminished by the integrated probability of finding the electron

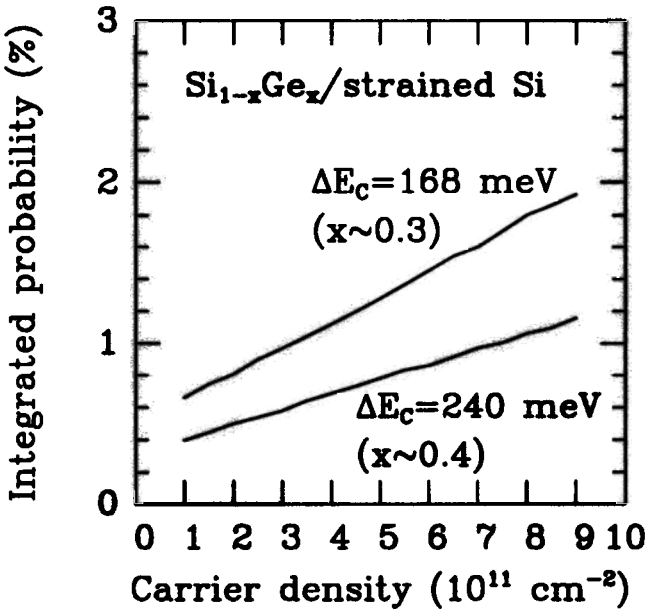

Figure 6.14: Integrated probability of finding an electron in the barrier as a function of carrier density in the 2DEG. Two different conduction band offsets, 168 meV and 240 meV, are used corresponding to 30% and 40% Ge content in the barrier respectively.

in the barrier, P_b. The actual expression becomes [6]

$$|M_{alloy}|^2 > \frac{\Omega_0}{S} x(1-x) {V_{alloy}}^2 \frac{\kappa_b {P_b}^2}{2} \tag{6.15}$$

where S is the sample area, Ω_0 is the atomic volume, and

$$\kappa_b = 2\sqrt{\frac{2m_z}{\hbar^2}(\Delta E_C - E_0)} \tag{6.16}$$

with ΔE_C being the conduction band offset and E_0 being the lowest confined state. The integrated probability, P_b, is plotted in Fig. 6.14 as a function of the carrier density for two different band offsets. As can be seen from the figure, it is of the order of a few percent.

To calculate the valley splitting, we need to substitute Eqn. 6.15 in Eqn. 6.14. However, the appearence of the sample area S is puzzling. Physically this arises because the wavefunctions are completely delocalized over the entire sample area and their interaction is that much weaker. In the evaluation of normal physical parameters

like mobility, the matrix element is multiplied by the density of states (which is proportional to the sample area) and S disappears in the final result. Therefore one concludes that the valley splitting is negligible in the absence of localization caused by an external influence like a magnetic field. In strong magnetic fields, the wavefunctions become localized over an area $\sim \lambda^2$ where $\lambda = \sqrt{\hbar/eB}$ is the magnetic length and B is the strength of the field. To first order, we replace S by λ^2 to obtain for the valley splitting in large magnetic fields[3]:

$$\Delta_{valley} \quad 2\sqrt{\frac{\Omega_0}{\hbar} eBx(1-x){V_{alloy}}^2 \frac{\kappa_b {P_b}^2}{2}} \tag{6.17}$$

The splitting varies as square root of the magnetic field. The calculations for a $Si_{0.7}Ge_{0.3}$ barrier with a band offset of 168 meV are shown in Fig. 6.15 for two different carrier densities. An alloy scattering potential of 800 meV for electrons was assumed in these calculations. Although the order of magnitude of the splitting energy (a few tenths of an meV) is correct, the experimental data obtained so far is insufficient for comparison. An ideal experimental structure to test the theory would be a high mobility modulation doped structure with a very dilute alloy channel (x $\sim$ 1%) so that the valley splitting can be enhanced without significantly degrading the mobility.

6.6.3 Maximum electron mobility in pure Si channels

In this section we calculate the maximum electron mobility in pure Si channels limited by alloy scattering in the barrier. The averaged square matrix element for this case is given by Eqn. 6.15. Substituting in Eqn. 2.16 we obtain for the mobility:

$$\mu_{alloy}^{barrier} \quad \frac{e\hbar^3}{m_{xy}^2 \Omega_0 {V_{alloy}}^2 x(1-x)} \frac{2}{\kappa_b {P_b}^2} \tag{6.18}$$

[3]Note that we have näively substituted $\sqrt{<|M_{alloy}|^2>}$ for $< \sqrt{|M_{alloy}|^2} >$. Also the correct harmonic oscillator wavefunctions in strong magnetic fields should be used to calculate M_{alloy}.

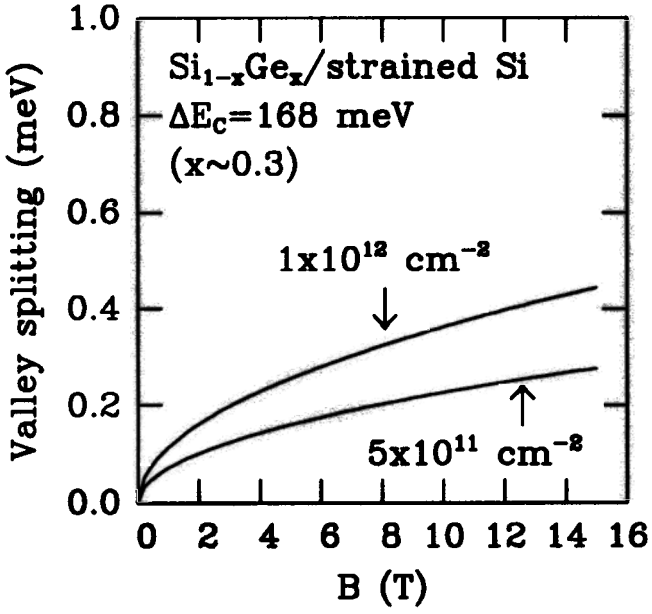

Figure 6.15: Calculations of the valley splitting Δ_{valley} as a function of the magnetic field for two different carrier densities. A $Si_{0.7}Ge_{0.3}$ barrier is assumed with an electron scattering potential of 0.8 eV.

Using the penetration probabilities calculated in Fig. 6.14, we estimate the alloy scattering limited mobilities in pure Si channels for electrons. The results are displayed in Fig. 6.16. The mobility decreases with increasing density and smaller band offsets. However, for typical Ge concentrations in the barrier ($x = 0.3 - 0.4$), they exceed 10^6 $cm^2/V \cdot s$. Hence the current maximum mobilities of $\sim$ 200,000 $cm^2/V \cdot s$ are probably limited by sample design and quality, leaving room for significant improvements in the future.

6.7 Conclusions

In this chapter we examined transport in $Si_{1-x}Ge_x$ strained alloy channels in detail. By comparing the experimental data with correct two dimensional scattering models incorporating multi-valley effects, we derived an alloy scattering potential of 0.8 eV for electrons and 0.6 eV for holes. From high-field measurements on bulk strained

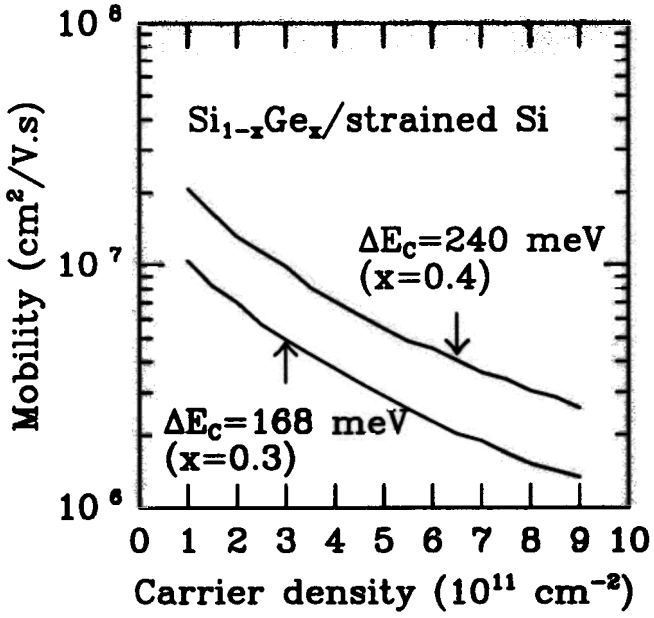

Figure 6.16: Mobility of the two-dimensional electron gas in pure Si channels limited by alloy scattering in the barrier. The mobility decreases with increasing carrier density and decreasing conduction band offset. Note that the numbers typically exceed 10^6 $cm^2/V \cdot s$.

$Si_{1-x}Ge_x$ layers at room temperature, V_{alloy} =0.6 eV for holes was derived by other workers [63] which agrees with our results. Perhaps the strongest evidence of alloy scattering limited transport is the recent demonstration by the AT&T group of *hole* mobilities exceeding 55,000 $cm^2/V \cdot s$ in *pure* Ge channels on relaxed $Si_{1-x}Ge_x$ substrates [64]. Finally, at the end of this chapter, we proposed theories involving alloy scattering, photoluminescence and magnetotransport which await further experimental support.

Chapter 7

Summary

7.1 Contributions to understanding of transport in SiGe alloys

In this section we summarise the important aspects of this thesis. The initial motivation was to examine the feasibility of modulation doping in the $Si/Si_{1-x}Ge_x$ strained material system. Both p-type and n-type modulation doped structures were successfully realized using the Rapid Thermal Chemical Vapor Deposition (RTCVD) growth system at Princeton. Using temperature dependent Hall measurements and quantum magnetotransport effects at low temperatures in high magnetic fields, we probed the band structure and the modifications induced by strain. By comparing the experimental results with current theoretical models, we were able to obtain valuable quantitative information about interface widths and doping changes on a monolayer scale in our samples. Using the two-dimensional hole gas as a probe in Chap. 3, we inferred an interface abruptness of 10 Å and suppression of boron segregation in our RTCVD environment. In the next chapter, we fabricated high mobility two-dimensional electron gases on novel "relaxed substrates" with low threading dislocation densities. Using optimized structures, we achieved high carrier densities and record low sheet resistivities (140 $\Omega/\Box$ at 77 K and 69 $\Omega/\Box$ at 10 K). By modifying these structures to incorporate a Schottky gate, we were able to modulate the carrier

density. In Chap. 5 we developed a novel two-mask processing scheme to fabricate MODFETs with completely self-aligned gates and low gate leakage currents at room temperature. The transconductance of these devices was limited severely by parasitic contact resistance due to non-optimized contacting schemes. The successful fabrication of MODFET structures, however, turned out to be extremely useful to further study low temperature transport of the two dimensional gas. Using gated structures in Chap. 6 we showed for the first time that the low mobility of holes in $Si_{1-x}Ge_x$ alloy channels vis-a-vis electrons in pure Si channels was due to a strong alloy scattering mechanism present in this material system. By comparing the experimental mobility degradation in specially designed structures with two-dimensional scattering models incorporating the multi-valley structure of $Si_{1-x}Ge_x$, we derived the first empirical alloy potentials for lateral transport of electrons (0.8 eV) and holes (0.6 eV) in strained $Si/Si_{1-x}Ge_x$ heterostructures. These are important parameters to model transport in $Si_{1-x}Ge_x$ based devices. Finally the insight offered by intervalley scattering due to alloy randomness led us to propose theories linking photoluminescence, low-field mobility and high magnetic field transport.

7.2 Directions for future work

This work raises some specific questions concerning our growth system. What is the mechanism limiting our maximum low temperature hole mobilities to below the theoretical calculations including alloy scattering ? If it is clear that background doping limits our electron mobilities, it is also obvious that any future thrust should concentrate on reducing contamination either by introducing additional gas purification or by changing growth conditions. In the MODFET area there is need to modify the contacting scheme, either by introducing ion implantantion or heavily doped regions under contact areas, to improve the transconductance and realize the full potential

of the self-aligned process.

The study on alloy scattering raises more general issues. The microscopic origin of the alloy scattering potential V_{alloy} is not well understood. Specifically, does this number depend on strain ? Does it vary with alloy composition ? More experiments on gated electron and hole gases may provide a clue. Finally, what is the maximum mobility achievable in this material system ? The history of GaAs/AlGaAs modulation doped structures shows that advances in growth techniques continue to provide samples with higher and higher mobilities. The high quality of the samples led to the discovery of a spectacular array of quantum mechanical effects never seen before. With the unique nature of strain and multi-valley bands, one would imagine that the same holds true for the $Si/Si_{1-x}Ge_x$ system.

References

[1] D.W. Greve, "Growth of epitaxial germanium-silicon heterostructures by chemical vapor deposition," *Materials Science and Engineering*, vol. B18, p. 22, 1993.

[2] G.C. Osburn, "Strained layer superlattices from lattice mismatched materials," *J. Appl. Phys.*, vol. 53, p. 1586, 1982.

[3] R. Dingle, H.L. Störmer, A.C. Gossard, and W. Wiegmann, "Electron mobilities in modulation-doped semiconductor heterostructure superlattices," *Appl. Phys. Lett.*, vol. 33, p. 665, 1978.

[4] T. Ando, A.B. Fowler, and F. Stern, "Electronic properties of two-dimensional systems," *Rev. Mod. Phys.*, vol. 54, p. 437, 1982.

[5] C. Weisbuch and B. Vinter, *Quantum semiconductor structures.* Academic Press, Sunset Beach, CA, 1991. Chap. 2, p. 38.

[6] G. Bastard, *Wave mechanics applied to semiconductor heterostructures.* Halsted Press, New York, NY, 1988. Chap. 6.

[7] B.K. Ridley, *Quantum processes in semiconductors.* Oxford University Press, New York, 1982.

[8] T. Ando, "Self-consistent results for GaAs/$Al_xGa_{1-x}As$ heterojunction. II. Low temperature mobility," *J. Phys. Soc. Japan*, vol. 51, p. 3900, 1982.

[9] R.E. Prange and S.M. Girvin, eds., *The quantum hall effect.* Springer-Verlag, New York, 2 ed., 1990.

References

[10] C.G. van de Walle and R.M. Martin, "Theoretical calculations of heterojunction discontinuities in the Si/Ge system," *Phys. Rev. B*, vol. 34, pp. 5621–5634, 1986.

[11] D.V. Lang, R. People, J.C. Bean, and A.M. Sergent, "Measurement of the band gap of Ge_xSi_{1-x}/Si strained-layer heterostructures," *Appl. Phys. Lett.*, vol. 47, p. 1333, 1985.

[12] K. Nauka, T.I. Kamins, J.E. Turner, C.A. King, J.L Hoyt, and J.F. Gibbons, "Admittance spectroscopy measurements of band offsets in $Si/Si_{1-x}Ge_x/Si$ heterostructures," *Appl. Phys. Lett.*, vol. 60, p. 195, 1992.

[13] J.C. Sturm, E.J. Prinz, P.M. Garone, and P.V. Schwartz, "Band-gap shifts in silicon-germanium heterojunction bipolar transistors," *Appl. Phys. Lett.*, vol. 54, p. 2707, 1989.

[14] J.C. Sturm, H. Manoharan, L.C. Lenchyshyn, M.L. Thewalt, N.L Rowell, J.P. Noel, and D.C. Houghton, "Well-resolved band-edge photoluminescence of excitons confined in strained $Si_{1-x}Ge_x$ quantum wells," *Phys. Rev. Lett.*, vol. 66, p. 1362, 1991

[15] X. Xiao, C.W. Liu, J.C. Sturm, L.C. Lenchyshyn, and M.L.W. Thewalt, "Photoluminescence from electon-hole plasmas confined in $Si/Si_{1-x}Ge_x/Si$ quantum wells," *Appl. Phys. Lett.*, vol. 60, p. 1720, 1992.

[16] R. People, "Physics and applications of Ge_xSi_{1-x}/Si strained layer heterostructures," *Appl. Phys. Lett.*, vol. 22, p. 1696, 1986.

[17] G. Schuberth, F. Schäffler, M. Besson, G. Abstreiter, and E. Gornik, "High electron mobility in modulation-doped Si/SiGe quantum well structures," *Phys. Lett.*, vol. 59, p. 3318, 1991.

[18] U. Gennser, V.P. Kesan, D.A. Syphers, T.P. Smith III, S.S. Iyer, and E.S. Yang, "Probing band structure anisotropy in quantum wells via magnetotunneling," *Phys. Rev. Lett.*, vol. 67, p. 3828, 1991.

[19] G. Abstreiter, H. Brugger, T. Wolf, H. Jorke, and H.J. Herzog, "Strain-induced two-dimensional electron gas in selectively doped Si/Si_xGe_{1-x} superlattices," *Phys. Rev. Lett.*, vol. 54, p. 2441, 1985.

[20] J.C. Sturm, P.V. Schwartz, E.J. Prinz, and H. Manoharan, "Growth of $Si_{1-x}Ge_x$ by rapid thermal chemical vapor deposition and application to heterojunction bipolar transistors," *J. Vac. Sci. Technol. B*, vol. 9, p. 2011, 1991.

[21] J.C. Sturm, P.M. Garone, and P.V. Schwartz, "Temperature control of silicon-germanium alloy epitaxy growth on silicon substrate by infrared transmission," *J. Appl. Phys.*, vol. 69, p. 542, 1990.

[22] P.V. Schwartz and J.C. Sturm, "Microsecond carrier lifetimes in strained silicon-germanium alloys grown by rapid thermal chemical vapor deposition," *Appl. Phys. Lett.*, vol. 57, p. 2004, 1990.

[23] P.M. Garone, J.C. Sturm, P.V. Schwartz, S.A. Schwarz, and B.J. Wilkens, "Silicon vapor phase epitaxial growth catalysis by the presence of germane," *Appl. Phys. Lett.*, vol. 56, p. 1275, 1990.

[24] J.C. Sturm and E.J. Prinz, "Graded base $Si/Si_{1-x}Ge_x/Si$ heterojunction bipolar transistors grown by rapid thermal chemical vapor deposition with near-ideal electrical characteristics," *IEEE Electron Device Lett.*, vol. 12, p. 303, 1991.

[25] E.J. Prinz and J.C. Sturm, "Current gain-Early voltage products in heterojunction bipolar transistors with nonuniform base bandgaps," *IEEE Electron Device Lett.*, vol. 12, p. 661, 1991.

[26] R. People and J.C. Bean, "Calculation of critical layer thickness versus lattice mismatch for Ge_xSi_{1-x}/Si strained-layer heterostructures," *Appl. Phys. Lett.*, vol. 47, p. 322, 1985.

[27] R. People, J.C. Bean, D.V. Lang, A.M. Sergent, H.L. Störmer, K.W. Wecht, R.T. Lynch, and K. Baldwin, "Modulation doping in Ge_xSi_{1-x}/Si strained layer heterostructures," *Appl. Phys. Lett.*, vol. 45, p. 1231, 1984.

[28] P.J. Wang, B.S. Meyerson, F.F. Fang, J. Nocera, and B. Parker, "High hole mobility in Si/$Si_{1-x}Ge_x$/Si p-type modulation-doped double heterostructures," *Appl. Phys. Lett.*, vol. 55, p. 2333, 1989.

[29] T. Mishima, C.W. Fredriksz, G.F.A. van de Walle, D.J. Gravesteijn, R.A. van den Heuvel, and A.A. van Gorkum, "Effect of interface quality on the electrical properties of p-Si/SiGe two-dimensional hole gas systems," *Appl. Phys. Lett.*, vol. 57, p. 2567, 1990.

[30] F.F. Fang, P.J. Wang, B.S. Meyerson, J.J. Nocera, and K.E. Ismail, "Two-dimensional hole gas in Si/SiGe heterostructures," *Surf. Sci.*, vol. 263, p. 175, 1992.

[31] J.-P. Cheng, V.P. Kesan, D.A. Grutzmacher, T.O. Sedgwick, and J.A. Ott, "Cyclotron resonance studies of two-dimensional holes in strained $Si_{1-x}Ge_x$/Si quantum wells," *Appl. Phys. Lett.*, vol. 62, p. 1522, 1993.

[32] M. Liehr, C.M. Greenlief, M. Offenberg, and S.R. Kasi, "Equilibrium surface hydrogen coverage during silicon epitaxy using SiH_4," *J. Vac. Sci. Technol. A*, vol. 8, p. 2960, 1990.

[33] Z. Matutinovic-Krstelj, J.C. Sturm, and E. Chason, "Growth pressure effects on $Si/Si_{1-x}Ge_x$ chemical vapor depostion," *Electronic Materials Conference*, 1993. Santa Barbara, June.

[34] D.W. Smith, C.J. Emeleus, R.A. Kubiak, E.H.C. Parker, and T.E. Whall, "Growth studies on $Si_{0.8}Ge_{0.2}$ channel two-dimensional hole gases," *Appl. Phys. Lett.*, vol. 61, p. 1453, 1992.

[35] Y.J. Mii, Y.H. Xie, E.A. Fitzgerald, D. Monroe, F.A. Thiel, B.E. Weir, and L.C. Feldman, "Extremely high electron mobility in Si/GeSi structures grown by molecular beam epitaxy," *Appl. Phys. Lett.*, vol. 59, p. 1611, 1991.

[36] F. Schäffler, D. Többen, H-J. Herzog, G. Abstreiter, and B. Holländer, "High-electron-mobility Si/SiGe heterostructures: influence of the relaxed SiGe buffer layer," *Semicond. Sci. Technol.*, vol. 7, p. 260, 1992.

[37] S.F. Nelson, K. Ismail, J.J. Nocera, F.F. Fang, E.E. Mendez, J.O. Chu, and B.S. Meyerson, "Observation of the fractional quantum Hall effect in Si/SiGe heterostructures," *Appl. Phys. Lett.*, vol. 61, p. 64, 1992.

[38] K. Ismail and S.F. Nelson and J.O. Chu and B.S. Meyerson, "Electron transport properties of Si/SiGe heterostructures: measurements and device implications," *Appl. Phys. Lett.*, vol. 63, p. 660, 1993.

[39] E.A. Fitzgerald, Y.H. Xie, M.L. Green, D. Brasen, A.R. Kortan, J. Michel, Y.J. Mii, and B.E. Weir, "Totally relaxed Ge_xSi_{1-x} layers with low threading dislocation densities grown on Si substrates," *Appl. Phys. Lett.*, vol. 59, p. 1611, 1991.

[40] F.K. LeGoues, B.S. Meyerson, and J.F. Morar, "Anamolous strain relaxation in SiGe thin films and superlattices," *Phys. Rev. Lett.*, vol. 66, p. 2903, 1991.

[41] A.H. Krist, D.J. Godbey, and N.P. Green, "Selective removal of a $Si_{0.7}Ge_{0.3}$ layer from Si(100)," *Appl. Phys. Lett.*, vol. 58, p. 1899, 1991.

[42] F. Stern and S.E. Laux, "Charge transfer and low-temperature electron mobility in a strained Si layer in relaxed $Si_{1-x}Ge_x$," *Appl. Phys. Lett.*, vol. 61, p. 1110, 1992.

[43] S.F. Nelson, K. Ismail, T.N. Jackson, J.J. Nocera, J.O. Chu, and B.S. Meyerson, "Systematics of electron mobility in Si/SiGe heterostructures," *Appl. Phys. Lett.*, vol. 63, p. 794, 1993.

[44] E.F. Crabbe, J.H. Comfort, W. Lee, J.D. Cressler, B.S. Meyerson, A.C. Megdanis, J.Y.C. Sun, and J.M.C. Stork, "73-GHz self-aligned SiGe-Base bipolar transistors with phosphorous-doped polysilicon emitters," *IEEE Electron Device Lett.*, vol. 13, p. 229, 1992.

[45] A. Gruhle and H. Kibbel and U. König and U. Erben and E. Kasper, "MBE-grown Si/SiGe HBT's with high β, f_T and f_{max}," *IEEE Electron Device Lett.*, vol. 13, p. 206, 1992.

[46] D.K. Nayak, J.C.S. Woo, J.S. Park, K.L. Wang, and K.P. MacWilliams, "Enhancement-mode quantum-well Ge_xSi_{1-x} PMOS," *IEEE Electron Device Lett.*, vol. 12, p. 154, 1991.

[47] P.M. Garone, V. Venkataraman, and J.C. Sturm, "Hole mobility enhancement in MOS-Gated Ge_xSi_{1-x}/Si heterostructure inversion layers," *IEEE Electron Device Lett.*, vol. 13, p. 56, 1992.

[48] U. König, A.J. Boers, F. Schäffler, and E. Kasper, "Enhancement mode n-channel Si/SiGe MODFET with high intrinsic transconductance," *Electron. Lett.*, vol. 28, p. 160, 1992.

References

[49] K. Ismail, B.S. Meyerson, S. Rishton, J. Chu, S. Nelson, and J. Nocera, "High transconductance n-type Si/SiGe modulation doped field effect transistors," *IEEE Electron Device Lett.*, vol. 13, p. 229, 1992.

[50] S.M. Sze, *Physics of semiconductor devices.* John Wiley, New York, NY, 1981

[51] K. Ismail, S. Rishton, J.O. Chu, K. Chan, and B.S. Meyerson, "High performance Si/SiGe n-type modulation doped transistors," *IEEE Electron Device Lett.*, vol. 14, p. 348, 1993.

[52] M. Glicksman, "Mobility of electrons in germanium-silicon alloys," *Phys. Rev.*, vol. 111, p. 125, 1958.

[53] T.P. Pearsall, ed., *GaInAsP alloy semiconductors.* Wiley, New York, NY, p.189.

[54] K. Hirakawa and H. Sakaki, "Mobility of the two-dimensional electron gas at selectively doped n-type $Al_xGa_{1-x}As$/GaAs heterojunctions with controlled electron concentrations," *Phys. Rev. B*, vol. 33, p. 8291, 1986.

[55] X. Xiao, *Silicon-germanium alloys for optoelectronic applications.* PhD thesis, Princeton University, 1993.

[56] O.J. Glembocki and F.H. Pollak, "Calculation of the Γ Δ electron-phonon and hole-phonon matrix elements in silicon," *Phys. Rev. Lett.*, vol. 48, p. 413, 1982.

[57] J. Weber and M.I. Alonso, "Near-band-edge photoluminescence of Si-Ge alloys," *Phys. Rev. B*, vol. 40, p. 5683, 1989.

[58] L.D. Laude, F.H. Pollak, and M. Cardona, "Effects of uniaxial stress on the indirect exciton spectrum of silicon," *Phys. Rev. B*, vol. 3, p. 2623, 1971

[59] S.L. Richardson, M.M. Dacorogna, F.H. Pollak, and M.L. Cohen, "First-principles calculation of the $\Gamma - X$ electron(hole) phonon matrix elements in silicon," *18th International Conference on the Physics of Semiconductors*, vol. 2, p. 1353, 1986.

[60] X. Xiao, C.W. Liu, J.C. Sturm, L.C. Lenchyshyn, and M.L.W. Thewalt, "Quantum confinement effects in strained silicon-germanium alloy quantum wells," *Phys. Lett.*, vol. 60, p. 2135, 1992.

[61] D. Monroe, Y.H. Xie, E.A. Fitzgerald, and P.J. Silverman, "Quantized hall effects in high-electron-mobility Si/Ge structures," *Phys. Rev. B*, vol. 46, p. 7935, 1992.

[62] T.S. Lay, J.J. Heremans, Y.W. Suen, M.B. Santos, K. Hirakawa, M. Shayegan, and A. Zrenner, "High-quality two-dimensional electron system confined in an AlAs quantum well," *Appl. Phys. Lett.*, vol. 62, p. 3120, 1993.

[63] S.H. Li, J.M. Hinckley, J. Singh, and P.K. Bhattacharya, "Carrier velocity-field characteristics and alloy scattering potential in $Si_{1-x}Ge_x/Si$," *Appl. Phys. Lett.*, vol. 63, p. 1393, 1993.

[64] Y.H. Xie, D. Monroe, E.A. Fitzgerald, P.J. Silverman, F.A. Thiel, and G.P. Watson, "Very high mobility two-dimensional hole gas in $Si/Ge_xSi_{1-x}/Ge$ structures grown by molecular beam epitaxy," *Appl. Phys. Lett.*, vol. 63, p. 2263, 1993.

Appendix A

Log-book of 2DHG samples

In this appendix, we summarise the growth details of all the p-type modulation doped structures. We also speculate on why some of them failed to work as expected. Before the active epitaxial layers were grown, all samples were subjected to a 1000°C 250 torr clean for 1 min, followed by a 1000°C 6 torr high- temperature Si buffer for 5 min. The growth pressure was 6 torr and the phosphine source was never used. Unless specified otherwise, n-type substrates ($\sim$ 1 Ωcm) were used.

Samples #328–334

These samples were grown on *p*-type wafers. Substrate conductivity remained fairly high at low temperatures, completely masking any effect of the 2DHG. With p-type Aluminum ohmic contacts, typical textbook mobility-temperature curves corresponding to $\sim 10^{16}$ cm^{-3} bulk doping were measured. For all subsequent samples, use n-type substrates.

Sample #369

time sec	temp °C	DCS sccm	GeH_4 sccm	B_2H_6 sccm	thickness Å	description
780	700	26		25	400	supply layer
495	625	26	129		800	$Si_{0.8}Ge_{0.2}$ channel
780	700	26		25	400	supply and cap

Symmmetric double heterostructure without spacers. Initially tried evaporated Al contacts annealed at 500°C for 30 min in the furnace. Contacts were good at room temperature, but non-linear at 77 K. Annealed at higher temperature 550°C for 20 min. Contacts now good at low temperature. Mobility at 10 K $\sim$ 380 $cm^2/V \cdot s$ and density $\sim 6 \times 10^{12}$ cm^{-2} . Increase spacer next time.

Sample #370

time sec	temp °C	DCS sccm	GeH_4 sccm	B_2H_6 sccm	thickness Å	description
780	700	26		25	400	supply layer
	700	26			50	spacer
495	625	26	129		800	$Si_{0.8}Ge_{0.2}$ channel
	700	26			50	spacer
780	700	26		25	400	supply and cap

Symmetric double heterostructure with 50 Å spacers. After 1:50 HF dip, evaporate 1000 Å Al and etch to form contacts. Anneal 550°C 15 min in nitrogen. Contacts are good at 10 K. Growth rate for Si at 700°C was assumed to be 25 Å/min. It is now estimated to be closer to 30 Å/min. This sample is discussed extensively in Chap. 3.

Sample #371

time sec	temp °C	DCS sccm	GeH_4 sccm	B_2H_6 sccm	thickness Å	description
780	625	26	129	25	1300	doped $Si_{0.8}Ge_{0.2}$ layer

Uniformly doped $Si_{0.8}Ge_{0.2}$ layer for comparison with 2DHG mobility. Same contact procedure. Carrier density $\sim 1.4 \times 10^{14}$ cm^{-2} and mobility $\sim$ 30 $cm^2/V \cdot s$ independent of temperature upt 10 K. Typical degenerately doped behaviour.

Sample #476

time sec	temp °C	DCS sccm	GeH_4 sccm	B_2H_6 sccm	thickness Å	description
480	625	26	129		800	$Si_{0.8}Ge_{0.2}$ channel
120	700	26			60	spacer
780	700	26		8	400	doped supply and cap layer

Single heterojunction with 60 Å spacer. The doping was reduced to 8 sccm flow. Standard Al contact procedure failed. Tried In contacts with 425°C 4 min anneal in forming gas. Did not work. Tried implanting BF_2^+ 2×10^{15} cm^{-2} 100 Kev. Annealed implant 680°C for 10 min. Contacts again non-linear. Finally tried Ti/Au contact which also failed. Suspect top layer doping insufficient ($< 10^{18}$ cm^{-3}).

Samples #477–478

These two samples had the same structure as #476 but different spacers and Ge contents. Cap layer doping (8 sccm) was again insufficient and all the above contact procedures failed.

Sample #482

time sec	temp °C	DCS sccm	GeH_4 sccm	B_2H_6 sccm	thickness Å	description
75	700	26		10	38	doped supply layer
170	700	26			85	spacer
40	625	26	400		160	$Si_{0.65}Ge_{0.35}$ channel
170	700	26			85	spacer
75	700	26		10	38	doped supply layer
450	700	26			225	undoped cap
135	700	26		10	65	doped cap
450	700	26			225	undoped cap

Symmetric double heterojunction with undoped cap structure. Doping has been increased to 10 sccm from previous run. Al contacts with 550°C 20 min anneal work well at 10 K. Low temperature mobility and carrier density are 1500 $cm^2/V \cdot s$ and 1.3×10^{12} cm^{-2} . Ge content in the channel probably too high.

Sample #513

time sec	temp °C	DCS sccm	GeH_4 sccm	B_2H_6 sccm	thickness Å	description
75	700	26		10	38	doped supply layer
	700	26			150	spacer
	625	26	42		400	$Si_{0.87}Ge_{0.13}$ channel
	700	26			600	undoped cap
300	700	26		30	150	heavily doped cap

First inverted 2DHG sample with 150 Å spacer. Cap doping was increased to 30 sccm. Al contacts good, but 10 K mobility ~ 80 $cm^2/V \cdot s$ and density $\sim 9 \times 10^{12}$ cm^{-2} almost independent of temperature. Shows signs of degenerate doping. Cap doping too heavy ?

Sample #514

time sec	temp °C	DCS sccm	GeH_4 sccm	B_2H_6 sccm	thickness Å	description
450	625	26	42		400	$Si_{0.87}Ge_{0.13}$ channel
	700	26			150	spacer
75	700	26		10	38	doped supply layer
300	700	26			150	undoped cap
300	700	26		20	150	heavily doped cap

Normal 2DHG structure nominally identical to #513. The cap layer doping was reduced to 20 sccm. Al contacts 550°C 25 min anneal in nitrogen good to low tem-

peratures. This sample was discussed in detail in Chap. 3. It now appears that the diborane flow has to be between 10 and 25 sccm for successful modulation doping.

Sample #528

Normal 2DHG structure identical to #514. Switched on DCS purifier. Bad contacts ! Tried other contacting schemes. Not successful. No idea why.

Sample #529

Inverted 2DHG structure identical to #513 *except* topmost layer doping flow reduced to 20 sccm. Again DCS purifier was switched on. Standard Al contact procedure successful and good modulation doping behaviour obtained. Results discussed in Chap. 3.

Sample #530

time sec	temp °C	DCS sccm	GeH_4 sccm	B_2H_6 sccm	thickness Å	description
75	700	26		10	38	doped supply layer
	700	26			150	spacer
10	700		370		15	pure Ge channel
	700	26			600	undoped cap
300	700	26		20	150	doped cap

Tried to grow pure Ge channel to suppress alloy scattering. Al contacts ohmic at room temperature, but resistance increases (while remaining linear) as temperature is lowered. At 10 K contacts are open (> 50 MΩ). Suspect 2DHG freezes out due to bad Si/Ge interface. Growth temperature for pure Ge probably too high.

Samples #550, #559 and #560

These samples were grown similar to the successful #370, #514 and #529 structures. Contacts were ohmic at 300 K but open at 10 K. 2DHG shows signs of freezing out. Later discovered that some samples grown during this period showed extraordi-

narily high ($\sim 10^{21}$ cm^{-3}) O_2 contamination by SIMS. Suspect large number of deep levels introduced by the O_2 causes 2DHG freeze-out.

Samples #627–628

These samples were grown on heavily doped $n^+ \sim 0.01$ Ωcm wafers for backgating studies. No colored rings were observed after growth on either wafer. Suspect no growth took place. Confirmed by X-ray microanalysis and bevel & stain technique. Temperature calibration curve probably incorrect for heavily doped wafers.

Appendix B

Log-book of 2DEG samples

This is a summary of n-type modulation doped structures using pure Si strained channels on a thick, graded relaxed buffer. A cleaning step consisting of a 2 min bake at 1000°C 250 torr followed by a 10 min 1000°C buffer was performed on all samples prior to the relaxed buffer growth. All samples were grown on p-type wafers ($\sim$ 10 Ωcm) and the diborane source was never turned on.

Sample #893

time sec	temp °C	DCS sccm	GeH_4 sccm	PH_3 sccm	thickness Å	description
3000	625	26	0–31		1000	0–10% grading
	625	26	31–100		2500	10–20% grading
	625	26	100–450		2600	30–38% grading
	625	26	450		6000	uniform $Si_{0.62}Ge_{0.38}$ layer
	800					anneal relaxed buffer at 6 torr
	700	26			75	strained Si channel
55	625	26	450	100	300	doped supply and cap layer

Modulation doped structure without spacer. Surface morphology was hazy with dense cross-hatch pattern. Tried Al contact initially used for 2DHG structures. Made good contact to p-type substrate but bad contact to 2DEG. Obtain n-type contact

B. Log-book of 2DEG samples

recipe using Au:Sb from Dr.Y.H. Xie. Au:Sb wire (with 0.8% Sb) was evaporated and annealed at 330°C for 10 min in forming gas. Good ohmic contacts, but Sb which evaporates first has adhesion problems to the SiGe. Later add an inital Au layer to promote adhesion. Measure n-type from sign of Hall voltage. Temperature dependent measurements are described in Chap. 4.

Sample #894

This sample was grown identical to #893 except that the relaxed buffer was annealed at 800°C for 1 hour in a reactor pressure of 680 torr. Surface turned out to be shiny. But contacts were non-linear even at room temperature. Is it because of the high-pressure anneal ?

Sample #907

time sec	temp °C	DCS sccm	GeH_4 sccm	PH_3 sccm	thickness Å	description
3000	625	26	0–31		1000	0–10% grading
2400	625	26	31–100		2500	10–20% grading
780	625	26	100–450		2600	30–38% grading
1200	625	26	450		6000	uniform $Si_{0.62}Ge_{0.38}$ layer
3600	800					anneal relaxed buffer at 6 torr
150	700	26			75	strained Si channel
8	625	26	450		40	spacer
55	625	26	450	100	300	doped supply and cap layer

Modulation doped structure with 40 Å spacer. Relaxed buffer annealed at 6 torr. Sample surface hazy. Good Au:Sb ohmic contacts down to low temperature. sample has been investigated in detail in Chap. 4.

Sample #908

Grown identical to #907 except that the relaxed buffer was annealed at 680 torr. Once again, sample surface was shiny and contacts were bad at room temperature.

Behaviour is similar to sample #894. It is now convincing that the high pressure anneal has a strong effect on the sample's electrical behaviour although it is not known what this effect is.

Sample #909

Similar to #907 with the same spacer and channel, but top layer doping flow reduced to 14 sccm. Good Au:Sb contacts (annealed 330°C for 3 min). At 10 K a mobility $\sim$ 10,000 $cm^2/V \cdot s$ and density $\sim 2.1 \times 10^{12}$ cm^{-2} was measured.

Sample #910

Similar to #907 except increase spacer to 80 Å . Au:Sb contacts good at low temperature. This sample had the highest mobility of 45,000 $cm^2/V \cdot s$ at 10 K. Details can be found in Chap. 4. The entire sequencer tables for the computer controlled growth of this sample are given in Appendix. D. Dopant flow of 100 sccm too high. Leads to parallel conduction in high magnetic fields. Reduce dopant flow next time.

Sample #911

time sec	temp °C	DCS sccm	GeH_4 sccm	PH_3 sccm	thickness Å	description
3000	625	26	0–31		1000	0–10% grading
	625	26	31–100		2500	10–20% grading
	625	26	100–450		2600	30–38% grading
	625	26	450		6000	uniform $Si_{0.62}Ge_{0.38}$ layer
	800					anneal relaxed buffer at 6 torr
120	700	26			60	strained Si channel
16	625	26	450		80	spacer
55	625	26	450	1	300	doped supply and cap layer

Modulation doped structure with 80 Å spacer. Identical to #910 except reduce doping to 1 sccm flow. Tried Au:Sb contacts annealed 330–450°C without success. Contacts non-linear at room temperature. Dopant flow is probably too low.

Sample #916

sec	temp °C	DCS sccm	GeH_4 sccm	PH_3 sccm	thickness Å	description
3000	625	26	0–31		1000	0–10% grading
2400	625	26	31–100		2500	10–20% grading
	625	26	100–450		2600	30–38% grading
1200	625	26	450		6000	uniform $Si_{0.62}Ge_{0.38}$ layer
	800					anneal relaxed buffer at 6 torr
150	700	26			75	strained Si channel
	625	26	450		600	spacer
55	625	26	450	100	300	doped supply and cap layer

Modulation doped structure with 600 Å spacer. Retain the high mobility #910 structure but increase spacer to reduce density and increase mobility. Did not open DCS purifier. Au:Sb contacts good. Low temperature density is 1.4×10^{12} cm^{-2} and mobility is 12,000 $cm^2/V \cdot s$. Density is too high for a 600 Å spacer indicating high background doping or parallel conduction.

Sample #922

Modulation doped structure with silane-grown channel. Sample identical to #910 except use SiH_4 to grow the channel in the hope of reducing background doping and improving mobility. But mobility ($\sim$ 38,000 $cm^2/V \cdot s$ at 10 K) and density ($\sim$ 1.6×10^{12} cm^{-2}) were very similar to that of sample #910.

Appendix C

Log-book of 2DEG samples with alloy channels and front gates

We describe here n-type modulation doped structure which were modified for alloy scattering and gated Hall measurements. Typically small amounts of Ge were added to the strained Si channel to enhance alloy scattering. The cap layer doping was reduced and an undoped cap was added for the gating experiments. The inital cleaning and growth of the buffer are described in Appendix.B.

Sample #1341

This sample was grown identical to #910 except that the spacer was increased to 100 Å . Au:Sb contacts were good, but the data showed presence of parallel conduction. This was removed by carefully etching the top layers and monitoring the room temperature density and mobility. The final measurements are shown in Chap. 6.

Sample #1343

time sec	temp °C	DCS sccm	GeH_4 sccm	PH_3 sccm	thickness Å	description
3000	625	26	0–31		1000	0–10% grading
	625	26	31–100		2500	10–20% grading
	625	26	100–450		2600	30–38% grading
1200	625	26	450		6000	uniform $Si_{0.62}Ge_{0.38}$ layer
	800					anneal relaxed buffer at 6 torr
90	625	26	40		75	strained $Si_{0.87}Ge_{0.13}$ channel
20	625	26	450		100	spacer
55	625	26	450	100	300	doped supply and cap layer

First 2DEG structure with 13% alloy channel. Spacer and doping identical to #1341. This sample showed even more parallel conduction effects because the 2DEG resistivity increased due to alloy scattering. The parallel conduction was removed by etching the cap layer. Measured data are discussed in Chap.6.

Sample #1344

Structure identical to #1343 except that the Ge content in the channel was increased to 20% (100 sccm GeH_4) while maintaining the channel thickness at 75 Å (asssuming a growth rate of 100 Å/min). Parallel conduction effect was solved by cap layer etching. Results are discussed in Chap.6.

Sample #1109

time sec	temp °C	DCS sccm	GeH_4 sccm	PH_3 sccm	thickness Å	description
3000	625	26	0–31		1000	0–10% grading
	625	26	31–100		2500	10–20% grading
	625	26	100–450		2600	30–38% grading
	625	26	450		3000	uniform $Si_{0.62}Ge_{0.38}$ layer
	800					anneal relaxed buffer at 6 torr
	700	26			75	strained Si channel
8	625	26	450		40	spacer
20	625	26	450	5	100	doped supply layer
80	625	26	450		400	undoped cap

Modulation doped structure with strained Si channel and undoped cap for front gating. The dopant flow was reduced to 5 sccm for complete depletion by the gate. The spacer is reduced to 40 Å for maximum carrier transfer. Au:Sb contacts and Al schottky gate were successful. The gating experiments are described in Chap. 6.4.

Sample #1380

time sec	temp °C	DCS sccm	GeH_4 sccm	PH_3 sccm	thickness Å	description
3000	625	26	0–31		1000	0–10% grading
	625	26	31–100		2500	10–20% grading
780	625	26	100–450		2600	30–38% grading
	625	26	450		3000	uniform $Si_{0.62}Ge_{0.38}$ layer
3600	800					anneal relaxed buffer at 6 torr
90	625	26	39		75	strained $Si_{0.88}Ge_{0.12}$ channel
8	625	26	450		40	spacer
20	625	26	450	10	100	doped supply layer
80	625	26	450		400	undoped cap

This sample used a 12% alloy channel and an undoped cap structure similar to #1109 for gating experiments. The doping in the supply layer was increased to 10 sccm to compensate for the lower band offset. However, although the Au:Sb contacts were good and a 2DEG was measured at 10 K, the Al Schottky gate could not change the carrier density before breakdown. Suspect the doping is too high for the gate to deplete completely. Have to reduce it back to 5 sccm.

Sample #1381

Modulation doping with $Si_{0.94}Ge_{0.06}$ channel and undoped cap. Growth procedure identical to #1380, except reduce GeH_4 flow to 18 sccm. Extrapolate Ge content to 6% and growth rate to $\sim$ 20 Å/min. Again the Au:Sb contacts showed presence of 2DEG at low temperature, but the Schottky gate could not modulate the carrier density. The 2DEG results are displayed in Table. 6.1.

Sample #1395

Sample structure identical to #1380 except reduce supply layer doping to 5 sccm. The cap structure is now similar to #1109 and both the contacts and the gate work well. Gated Hall measurements for this sample are discussed in Chap. 6.4.

Appendix D

Growth sequence of sample #910

Sequencer Table # 0

Step	*Action*	*Comment*
0	CONTROL ON&	turn on control
1	SCAN ON(0.3)	and scan simultaneously
2	SET(SP7,0)&	lamp power zero
3	SET(SP4,0)	turn off PID control
4	SET(SP0,0)	zero loop counter
5	SET(SP1,1)	not a superlattice
6	SET(DO0,1)	N_2 off
7	SET(DO2,0)&	selects off
8	SET(DO3,0)&	
9	SET(DO4,0)&	
10	SET(DO5,0)&	
11	SET(DO6,0)&	
12	SET(DO7,1)&	DCS sel on
13	SET(DO8,0)&	
14	SET(DO9,0)&	injects off
15	SET(DO10,0)&	
16	SET(DO11,0)&	

17	SET(DO12,0)&	
18	SET(DO13,0)&	
19	SET(AO1,0.01)	flow rates down
20	SET(AO2,0.213)	GeH_4 flow 100 sccm
21	SET(AO3,0.01)	
22	SET(AO4,0.01)	
23	SET(AO5,0.5)	
24	SET(AO6,0.538)	DCS flow 26 sccm
25	SET(AO7,0.01)	
26	SET(DO15,1)	vacuum on
27	SET(DO1,1)	H_2 on
28	SET(AO0,0.62)	H_2 flow 3 slpm
29	WAITUNTIL(AI24>0.5)	close LP;press Go for start
30	SEQUENCER ON(0.3,1,0)	start SEQUENCER # 1

Sequencer Table # 1

Step	*Action*	*Comment*
0	SET(AO11,0)	pressure guage : 1–1000 torr
1	SET(AO8,0.25)	set pressure to 250 torr
2	SET(AO0,0.8)	H_2 flow 4 slpm
3	WAITUNTIL(AI29>0.24)	
4	WAIT(10)	
5	WAITUNTIL(AI29<0.26)	wait for stable pressure
6	RAMP(SP7,0.4,0.274)	ramp up T to 1000°C
7	WAIT(120)	2 minutes clean
8	SET(AO0,0.62)	H_2 flow 3 slpm

9	SET(AO8,0.0)	pump down
10	WAITUNTIL(AI29<0.01)	wait until pressure < 0.01 torr
11	SET(AO11,1)	switch to 1–10 torr guage
12	WAITUNTIL(AI24>0.5)	open LP; press Go for buffer
13	SET(SP2,0)	
14	SEQUENCER ON(0.3,7,0)	call buffer layer sequencer #7
15	WAITUNTIL(SP2>0.5)	wait until seq 7 is done
16	SET(SP2,0)	
17	SEQUENCER ON(0.3,6,0)	call relaxed buffer sequencer #6
18	WAITUNTIL(SP2>0.5)	wait until seq 6 is done
19	SET(SP2,0)	
20	SEQUENCER ON(0.3,4,0)	call modulation doping sequencer #4
21	WAITUNTIL(SP2>0.5)	wait until seq 4 is done
22	SEQUENCER OFF(1)	end of growth

Sequencer Table # 7

Step	*Action*	*Comment*
0	SET(DO7,1)	DCS sel on
1	SET(AO6,0.538)	DCS flow 26 sccm
2	RAMP(SP7,0.4,0.274)	set T=1000°C
3	SET(AO8,0.6)	set pressure 6 torr
4	WAITUNTIL(AI28<0.61)	
5	WAIT(10)	
6	WAITUNTIL(AI28>0.59)	wait for pressure to stabilize
7	SET(DO13,1)&	inject DCS
8	WAIT(600)	High-T buffer

9	SET(DO13,0)&	DCS inject off
10	SET(DO3,1)	GeH_4 sel on
11	WAIT(10)	
12	RAMP(SP7,-0.4,0.0)	lamp off
13	SET(AO0,0.1)	H_2 flow down
14	WAITUNTIL(AI24>0.5)	press Go, switch 1.3 1 to 3
15	SET(SP3,1)	get cold values
16	WAIT(1)	
17	SET(SP3,0)	retain cold values
18	SET(AO2,0.213)	
19	SET(AO0,0.62)	H_2 flow 3 slpm
20	SET(SP2,1)	end of seq 7

Sequencer Table # 6

Step	*Action*	*Comment*
0	RAMP(SP7,0.4,0.274)	set T=1000°C
1	SET(DO7,1)&	select DCS
2	SET(DO3,1)&	select GeH_4
3	WAIT(10)	
4	SET(DO13,1)	inject DCS
5	WAIT(60)	High-T buffer
6	RAMP(SP7,-0.2,0.13)	T down to 625°C
7	WAIT(10)	
8	SET(SP5,2.419)&	setpoint T=625
9	SET(SP4,1)	PID on
10	WAIT(30)	

11	SET(AO2,0.01)	GeH_4 0 sccm
12	WAIT(10)	
13	SET(DO10,1)	inject GeH_4
14	RAMP(AO2,0.00156,0.078)	grade 0–10% 1000 Å
15	RAMP(AO2,0.0034,0.214)	grade 10–20% 2500 Å
16	RAMP(AO2,0.054,0.918)	grade 20–38% 2600 Å
17	WAIT(1200)	uniform buffer
18	SET(DO10,0)&	GeH_4 inj off
19	SET(DO13,0)	DCS inj off
20	WAIT(10)	
21	SET(SP4,0)	PID off
22	RAMP(SP7,0.4,0.199)	set T=800°C
23	WAIT(3300)	anneal; close selects manually
24	WAIT(300)	open both selects
25	RAMP(SP7,-0.2,0.14)	T down to 700°C
26	SET(SP2,1)	end of seq 6

Sequencer Table # 4

Step	*Action*	*Comment*
0	SET(AO6,0.538)&	DCS 26 sccm
1	SET(SP5,3.308)	setpoint T=700
2	SET(SP4,1)	PID on
3	SET(DO5,1)&	PH_3 sel on
4	WAIT(10)	
5	SET(AO4,0.213)	PH_3 high 100 sccm
6	SET(DO13,1)	DCS inj on
7	WAIT(150)	strained Si channel

8	SET(SP5,2.419)	setpoint T=625
9	WAIT(10)	
10	SET(DO10,1)	inject GeH_4
11	WAIT(16)	spacer 80 Å
12	SET(DO12,1)&	inj PH_3
13	WAIT(55)	Doped cap =:300 Å
14	SET(DO10,0)&	GeH_4 inj off
15	SET(DO3,0)&	GeH_4 sel off
16	SET(DO13,0)&	DCS inj off
17	SET(DO7,0)&	DCS sel off
18	SET(DO12,0)&	PH_3 inj off
19	SET(DO5,0)&	PH_3 sel off
20	WAIT(10)	
21	SET(SP9,0.1)	lamp down to 10%
22	SET(SP4,0)	PID off
23	RAMP(SP7,-0.4,0.0)	lamp off
24	SET(AO8,0.0)	
25	SET(SP2,1)	end of seq 4

Appendix E

Publications and Presentations resulting from this thesis

Journal articles

1. V. Venkataraman, C.W. Liu, and J.C. Sturm, " Alloy scattering limited transport of two-dimensional carriers in strained SiGe quantum wells", *Applied Physics Lett.*, **63**, 2795, (1993).

2. P.M. Garone, V. Venkataraman, and J.C. Sturm, "Hole mobility enhancement in MOS-gated GeSi/Si heterostructure inversion layers", *IEEE Electron Device Lett.*, **13**, 56, (1992).

3. P.M. Garone, V. Venkataraman, and J.C. Sturm, "Hole confinement in MOS-gated GeSi/Si heterostructures", *IEEE Electron Device Lett.*, **12**, 230, (1991).

4. V. Venkataraman, P.V. Schwartz, and J.C. Sturm, "Symmetric Si/SiGe two dimensional hole gases grown by rapid thermal chemical vapor deposition", *Applied Physics Lett.*, **59**, 2871, (1991) .

Conference presentations

1. Z. Matutinovic-Krstelj, E.J. Prinz, V. Venkataraman, and J.C. Sturm, "A comprehensive study of lateral and vertical current transport in $Si/Si/Si_{1-x}Ge_x/Si$

E. Publications and Presentations resulting from this thesis

HBT's", *International Electron Devices Meeting*, Washington D.C., December 1993.

2. V. Venkataraman, C.W. Liu, and J.C. Sturm, "Effect of alloy scattering on low temperature mobilities of two-dimensional holes and electrons in $Si/Si_{1-x}Ge_x$ heterostructures", *Electronic Materials Conference*, Santa Barbara, June 1993.

3. V. Venkataraman, C.W. Liu, and J.C. Sturm, "High mobility electron gases with very low sheet resistivities and MODFETs fabricated in SiGe/Si ", *AVS Topical Symposium on Silicon-based Heterostructures*, Chicago, November 1992.

4. J.C. Sturm, P.M. Garone, and V. Venkataraman, "High hole mobility p-channel MOSFET's using MOS-gated $Si/Si/Si_{1-x}Ge_x$ heterostructures", *Int. Conf. on Solid State Devices and Materials*, Yokohama, August 1991.

5. P.M. Garone, V. Venkataraman, and J.C. Sturm, "Hole mobility enhancement in MOS-gated $Si/Si_{1-x}Ge_x/Si$ heterostructure inversion layers", *Electronic Materials Conf.*, Boulder, June 1991.

6. V. Venkataraman and J.C. Sturm, "Single and symmetric double two-dimensional hole gases at Si/SiGe heterojunctions grown by rapid thermal chemical vapor deposition", *MRS Spring Meeting*, Anaheim, April 1991.

7. P.M. Garone, V. Venkataraman, and J.C. Sturm, "Carrier confinement in MOS-gated $Si/Si_{1-x}Ge_x/Si$ heterostructures", *International Electron Devices Meeting*, San Francisco, December 1990.

8. J.C. Sturm, P.M. Garone, E.J. Prinz, P.V. Schwartz, and V. Venkataraman, terface abruptness in epitaxial silicon and silicon-germanium structures grown by rapid thermal chemical vapor deposition", *Electrochemical Society International CVD Symposium*, Seattle, October 1990.

Conference papers

1. V. Venkataraman, C.W. Liu, and J.C. Sturm, "Effect of alloy scattering on low-temperature mobilities of two-dimensional holes and electrons in $Si/Si/Si_{1-x}Ge_x$ heterostructures", *Tech. Prog. Elec. Mat. Conf.*, 12 (1993).

2. V. Venkataraman, C.W. Liu, and J.C. Sturm, "High mobility electron gases and modulation doped field effect transistors fabricated in Si/SiGe by rapid thermal chemical vapor deposition", *J. Vac. Sci. Tech.B.*, **11**, 1176, (1993).

3. V. Venkataraman and J.C. Sturm, "Single and double two-dimensional hole gases at Si/SiGe heterojunctions grown by rapid thermal chemical vapor deposition", *Proc. Symp. Mat. Res. Soc.*, **220**, 391, (1991).

4. J.C. Sturm, P.M. Garone, and V.Venkataraman, "High hole mobility p-channel MOSFET's using MOS-gated $Si/Si/Si_{1-x}Ge_x$ heterostructures", *Proc. Int. Conf. on Solid State Devices and Materials*, 261, (1991).

5. J.C. Sturm, H. Manoharan, V. Venkataraman, P.V. Schwartz, and P.M. Garone, "Control of individual layer growth temperatures by rapid temperature switching in $Si/Si_{1-x}Ge_x$ multilayer structures grown by rapid thermal chemical vapor deposition", *Proc. Inter. Conf. on Elec. Mat.*, 457, (1990).

6. J.C. Sturm, P.M. Garone, E.J. Prinz, P.V. Schwartz, and V. Venkataraman, "Interface abruptness in epitaxial silicon and silicon-germanium structures grown by rapid thermal chemical vapor deposition", *Proc. of the Eleventh Inter. Conf. on Chemical Vapor Deposition*, 295, (1990).

7. P.M. Garone, V. Venkataraman, and J.C. Sturm, "Carrier confinement in MOS-Gated SiGe/Si quantum well structures", *Inter. Electron Devices Mtg. Tech. Dig.*, 383, (1990).